https://dx.doi.org/10.1016/j.tws.2022.109220

Investigations on material properties and residual stresses in cold-formed high strength steel irregular hexagonal hollow sections

Jun-zhi Liu[1], Han Fang[3], Tak-Ming Chan[1, 2, *]

[1] Department of Civil and Environmental Engineering, The Hong Kong Polytechnic University, Hong Kong, China
[2] Chinese National Engineering Research Centre for Steel Construction (Hong Kong Branch), The Hong Kong Polytechnic University, Hong Kong, China
[3] School of Civil, Environmental and Mining Engineering, The University of Adelaide, South Australia 5005, Australia
* Corresponding author: tak-ming.chan@polyu.edu.hk

Abstract

This paper presents an experimental investigation on the material properties variation and residual stress distribution within the cold-formed high strength steel (HSS) irregular hexagonal hollow sections (IHexHS) with two different fabrication methods. The test specimens were manufactured through press-braking and gas metal arc welding (GMAW). Tensile coupons tests were conducted on specimens fabricated from the critical locations within cold-formed HSS irregular hexagonal hollow sections, namely the flat portions, corner portions of either half or quarter sections. New material models to predict the material properties for the tensile coupons with both rounded responses and yield plateau followed by significant strain hardening were proposed. In conjunction with conventional tensile coupon testing, non-contact digital image correlation (DIC) measurement through which strain fields along the gauge length before and after the occurrence of diffuse necking was carried out to obtain the accurate strain field after necking. Moreover, the residual stresses measurements for HSS IHexHS were also performed, membrane and bending residual stresses distributions on the investigated sections were measured in longitudinal directions with 59 strips cut by wire-cutting method and more than 708 strain readings obtained. Results of the residual stress distributions and magnitudes are presented and discussed. Based on the measurement results, predictive models for residual stress distribution were developed and can be subsequently applied for predicting structural behaviour of the cold-formed HSS IHexHS.

Keywords: Cold-formed, Irregular hexagonal hollow sections; High strength steel; Residual stresses; Digital image correlation method; Material properties.

1. Introduction

With the technological advancement in material areas, high strength steel (HSS) with nominal yield strength higher than 460 MPa are commercially available worldwide [1–3]. The employment of the HSS can reduce the cross-sectional geometry of the structural members resulting in larger free floor space. The reduced structural sizes further generate benefits such as lower costs for transportation, assembly and construction, and reduced carbon footprint [4, 5]. Compared with mild steel material, which featured a linear elastic range, following by a pronounced yield plateau with a sharply defined yield point, HSS materials exhibit either relatively rounded response or well-defined yield plateau, primarily depending on manufacturing process and delivery conditions. HSS materials properties in HSS cold-formed sections usually exhibit rounded stress-strain response and lower level of strain-hardening [6]. Fabrication related processes including cold-forming such as press-braking and welding will induce residual stresses with different patterns and magnitudes that influence the structural performance of cold-formed steel members. Thus, good understanding of material properties and the residual stresses are crucial for structural analysis and design. Material properties and residual stresses distribution of HSS structures have been previously carried out with the main focus on built-up sections concerning welded box, I- and cruciform sections.

Numerous studies have been conducted concerning residual stresses in HSS built-up sections in past years. Nishino et al. [8] illustrated that the impact of residual stresses on the strength of box columns was less pronounced for the structures with varying plate width-to-thickness ratios (b/t) between 26 and 44 and made from HSS A514 plates (nominal yield strength = 690 MPa), comparing with their counterparts fabricated from mild steel. Usami and Fukumoto [9,10] performed residual stresses measurements on HSS welded box columns comprising A514 plate with b/t ratios varying between 22, 33, 44 and further expanded to 29, 44 and 58 respectively. The thicknesses of the plates for the welded box section specimens are 6 mm and 4.5 mm respectively. Rasmussen and Hancock [11] studied the residual stresses distribution in the cruciform sections with yield strength up to 690 MPa and found that b/t ratio has a significant effect on residual stresses distribution and magnitudes. The residual stresses distribution of box section fabricated using Q460 plates has been investigated by Wang et al. [12] and a trapezoidal model for predicting residual stress distribution and magnitudes are provided in the study. Furthermore, Ban et al. [13] found that the residual stresses remarkably depend on cross section geometry including the thickness and b/t ratio, which is different from the findings that b/t ratio has negligible impact on residual stresses [14]. Kim et al. [15] conducted investigation on residual stresses for welded box section of HAS 800 (nominal yield strength = 800 MPa) and found that the magnitudes of the residual stresses show independency of yield strengths of steel material. In contrast, Somodi and Kövesdi [16] subsequently studied the residual stresses distribution in HSS welded box sections and concluded that residual stresses depend on the yield strength as well as b/t ratio. Khan et al. [17] performed investigations on the residual stresses for HSS welded box sections using non-destructive neutron diffraction method and demonstrated that welding residual stresses existing in sections with thicker steel plates are generally higher than the one comprised of thinner steel plates.

In addition to the numerous studies for residual stresses in built-up steel structures, experimental investigations on residual stresses in HSS cold-formed sections have been extensively investigated in [18–21] including circular (CHS), square (SHS) and rectangular (RHS) hollow sections. Moreover, apart from these experimental studies, numerical investigations have also been performed on the residual stress distribution for HSS RHS and SHS in [7], and for the HSS elliptical hollow sections (EHS) in [22,23]. Furthermore, Wang et al. [3] studied hot-finished HSS hollow sections for SHS and RHS with yield strength ranging from 460 MPa to 690 MPa. Apart from the structures considered in these investigations with H, cruciform, CHS, RHS and SHS, increased interests have recently been focusing on the application of HSS polygonal sections which not only provide higher buckling resistance but also allow for easier connection construction with incoming members [24–29]. In particular, the application of hexagonal sections as part of the polygonal section family was successfully applied in high-rise buildings for their aesthetic performance and easier connection with beams and core tube as mega frame-core tubes [30], as depicted in Fig. 1. Nevertheless, the investigation of HSS cold-formed hexagonal sections is very limited. The experimental study on residual stress and material properties variation has been carried out in [31] on hexagonal sections (HexHS). No research investigation concerning for residual stress distribution of HSS irregular hexagonal sections (IHexHS) with internal angles of 90° and 135° has been carried out.

Cold-formed tubular sections can be fabricated through welding and press-braking processes which result in residual stress within the hollow sections. Press-braking process essentially altered the material response due to the excessive strain hardening associated with plastic deformation [13,32,33]. Theoretical and numerical studies of the impact of cold-forming and press-braking on cold-formed sections have been carried out in [34–38]. Additionally, the material properties are also invariably affected by welding, particular at the locations close to the welding seam. The material properties within the heat affected zone (HAZ) are different from those outside HAZ. Reduction in yield strength and ultimate strength can be observed linearly proportional to the linear heat input [39,40]. In addition, the welding induced thermal residual stresses together with residual stresses caused by cold-forming processes can also affect the structural behaviour of the members by causing premature yielding through part of the material thickness, consequently leading to overall instability of the structural members. Therefore, the understanding of the material properties and residual stresses distribution in HSS hexagonal hollow sections form the basis for accurate design and analysis of the structures.

The current design of steel hollow sections up to 690 MPa has been codified in EN 1993-1-12 [41], ANSI/AISC-360-16 [42]. However, the design guide related to hexagonal sections is not included in these standards. To facilitate the accurate prediction and design of the cold-formed HSS IHexHS members, the material properties and distribution and magnitude of the residual stresses for the sections are investigated in this paper. A total of 60 tensile coupons consisting of flat, corner and weld coupons were taken from the cold-formed HSS IHexHS and tensile tests were conducted to determine the stress-strain responses. Suitable stress-strain models for the materials at flat and corner portions were assessed and developed. The residual stress measurements were also performed on HSS cold-formed irregular hexagonal hollow sections with varying aspect ratios and parent plates of different thicknesses. A total of 59 strips were cut from the specimens with measurements of more than 708 strain readings. Based on the test results, the predictive models of the distribution of the residual stresses are proposed in this paper.

2. HSS cold-formed irregular hexagonal hollow section specimens

HSS plates of Q690 grade with a thickness of 6 mm and 10 mm were used for preparing cold-formed IHexHS specimens for the investigation. The chemical composition of the HSS plates is shown in Table 1. The high strength steel plates were longitudinally folded at room temperature through press braking by a hydraulic press-brake machine with a capacity up to 1200 Tons. To avoid the cracks along the bending area, the designed radius to thickness ratios met the requirements proposed in various international specifications in EN 10219-2 [43], GB/T 6728 [44], JIS G 3101 [45] and ASTM A1085 [46]. The inner radius to thickness ratio is 3 for 6 mm and 10 mm thick sections in this investigation, resulting in an inner radius of 18 mm and 30 mm respectively. After the completion of the press-braking process, the two cold-formed half sections were welded together using gas metal arc welding (GMAW) after filling the ceramic backing at the flat portion or corner and full penetration welding was applied using 1.2 mm electrode of ER110S-G category (f_y = 860 MPa, f_u = 920 MPa) in accordance with the specification AWS A5.28/5.28 M [47]. It is a common practice to use ER 100S-G and ER 110S-G for welding the Q690 steel and ER 110S-G is used to achieve the over-matched condition in this study. Chemical composition of these two types of electrodes can be seen in Table 2. The shielding gas mainly consisted of 80% Argon (Ar) with remaining volume filled with 20% carbon dioxide (CO_2) of 10 MPa filling pressure. The voltage, current and the welding speed were carefully controlled and recorded to determine the linear heat input energy. The current varied between 125 A and 192

A while the voltage was between 19 V and 23.8 V with welding speed measured and the generated linear heat input were derived and listed in Table 3.

The HSS cold-formed IHexHS in this study with welding regions appeared in corner area was defined as CF1 series whereas the sections with welding at flat portion, were defined as CF2 series. The geometry was defined using the nomenclature shown in Fig. 2. The nominal dimensions of HSS cold-formed IHexHS are (B_L× t × aspect ratio) 145 × 6-1.75, 220 × 6-2.00 and 145 × 10-1.75 with detailed dimensions and labels shown in Fig. 3. The measured dimensions are provided in Table 4, where B_s, b_s B_L, b_L, t, and r_i are the edge length, inclined short length, longer edge length, longer flat portion side length, thickness and the inner corner radius and the aspect ratio is defined as H/B. The nominal cross section aspect ratio of the specimens varies between 1.75 and 2.0 with plate width-to-thickness ratios ranging between 6.6 and 38.7. The specimens were labelled as "Series-nominal edge length B_L × thickness-aspect ratio". For example, the label CF1-145 × 6-1.75, represents the specimen fabricated with the first fabrication method with welding appeared in corner region [Fig. 2(a)] and with nominal longer edge length equal to 145 mm, nominal thickness equal to 6 mm and the aspect ratio of 1.75.

As per GB 50205 [49], the inspection of the quality of the weldment should be carried out to satisfy construction quality of steel structure. X-ray inspection was designed in accordance with GB/T 3323.1 [50] and ISO 17636-1 [51] and the obtained test results were assessed according to GB 50661 [52]. The adopted set-up of industrial X-ray inspection can be seen in Fig. 4. From the inspection, no crack, porosity, undercut and slag inclusion were observed from the welding part of the investigated specimens. Moreover, magnetic particle inspection method is employed to detect the possible crack near the corner portion and the weldment since it underwent severe plastic deformation and HAZ effect. No crack was observed near the corner portion and the weldment, indicating the suitable ratio of inner radius to thickness and well-controlled heat input from welding, as demonstrated in Fig. 5.

3. Material properties investigation

With the increasing use of HSS materials in structures and constructions worldwide, countries and regions have published standards on HSS structural design and material properties for HSS structural members. The specified limiting values on strength and ductility requirements in standards are summarized in Table 5. It should be noted that only requirements specified for Q690 or its equivalent strength are listed, although high strength steel on G65 (f_y = 450 MPa) in A852/852M [53], HSLA（f_y = 485 MPa）in A1085/1085M [46] and HPS 70W (f_y = 485 MPa) in A709/A709M-18 [54] were also provided. The heterogeneous material properties may exist in the examined HSS cold-formed irregular hexagonal sections due to the combined fabrication processes of welding and press-braking. The process of press-braking mainly causes enhancement of the yield strength and ultimate strength [32], whereas the material properties in the vicinity of the weldment are amply affected by the heat affected zone (HAZ). In order to investigate the variation of the material properties, the tensile coupons were machined from different regions within the HSS irregular hexagonal hollow sections. In addition, the tensile coupons were also extracted from the parent plates. The resultant material properties from these parent plate tensile coupons were compared with those measured for cold-formed HSS IHexHS in order to examine the impact of the fabrication processes.

3.1 Parent coupons

Six tensile coupons were taken from each batch of the parent steel plates in the longitudinal and transverse directions to examine the heterogeneity of the material properties of parent plates. All the tensile coupon tests were conducted in accordance with EN ISO 6892-1: 2019 [55] using an in-house electromechanical high force universal testing system of Instron 5982 testing machine with the capacity of 100 kN. The dimensions of the tensile coupons from parent plates were carefully designed in accordance with EN 6892-1: 2019 [55] with 13 mm and 8 mm width along a gauge length of 50 mm respectively for specimens extracted from 6 mm and 10 mm thick plates. According to EN ISO 6892-1:2019 [55] the proportional elongation at fracture (ε_f) is obtained based on an original gauge length of $5.65\sqrt{A}$, where A is cross-section area along the parallel original gauge length of the coupon. For each tensile coupon, the original gauge length was marked by fine lines before testing. An optical non-contact video extensometer with gauge length of either 25 mm or 50 mm painted by white dots was utilized to capture the full engineering stress-strain relationship. The elongation at fracture either 25 mm ($\varepsilon_{f,25}$) or 50 mm ($\varepsilon_{f,50}$) can be directly obtained from the video extensometer. As for coupons failed outside the effective range of the video extensometer, it was determined by carefully fitting the fractured pieces and comparing the final gauge length to the original gauge length. The test arrangement of the tensile coupon can be seen in Fig. 6. Four electrical strain gauges were affixed to the mid-length on both side of each coupon to determine the Poisson's ratio v, with averaged measured material properties summarized in Table 6, where $E_{s,p}$ indicates the elastic modulus of the parent steel plate, $f_{y,p}$ is yield strength, $f_{u,p}$ is the ultimate strength, $\varepsilon_{sh,p}$ is strain-hardening strain, $\varepsilon_{u,p}$ is strain at ultimate strength, $\varepsilon_{f,p}$ is elongation at fracture and $\varepsilon_{f,p}$ is the proportional elongation at fracture. Typical stress-strain curves of the parent plate can be seen in Fig. 7 with a letter "p" in subscript indicating it is the material properties from parent plate. A typical 10 mm parent tensile coupon after testing is presented in Fig. 9.

3.2 Flat and corner coupons

Flat coupons were machined from the centre of the flat portion of the hollow sections and all the coupon tests were performed using the same testing procedures as those applied to the tensile coupons from the parent plates. The flat and corner tensile coupons were machined with 4 mm and 8 mm width along the gauge length respectively for those from the sections with plate thicknesses of 6 mm and 10 mm. Two linear electrical strain gauges were adhered to the mid-length of each side of the coupon by which the modulus of elasticity (E_s) can be determined on the basis of the average measured strain. The material properties including 0.2% proof stress ($f_{0.2}$) or yield strength (f_y), ultimate tensile strength (f_u), the measured 0.05% proof stress ($f_{0.05}$), the strain hardening component n for flat coupon plate, strain-hardening strain (ε_{sh}), ultimate tensile strain (ε_u) and elongation at fracture (ε_f) of the material can be determined. The precise measurements of the strain field at necking region can be obtained by using digital image correlation method (DIC). The material properties measured for flat coupons taken from the IHexHS are presented in Table 7 to Table 10. Akin to the flat coupons, tensile testing on the corner tensile coupons was conducted in line with the guidance in EN 6892-1: 2019 [55]. The corner coupons were machined from the two corner regions of each hollow section with one corner of 90 degrees and the other one with 135 degrees. To minimize the effect of local eccentric load, the width of the corner coupons from sections with plate thickness of 6 mm was machined with 4 mm width along the gauge length. For those sections with thickness of 10 mm, the corner coupons were featured with 8 mm width along the gauge length. For each corner coupon, two holes with diameter of 10 mm were drilled at the distance of 20 mm from the end of the coupon, as verified according to EN 1993-1-8 [66]. A pair of specially developed grips with two pins was utilized to apply the tensile load through its centroid, as shown in Fig. 8. The stress was determined based on the cross-section area scanned from AutoCAD, as shown in Fig. 9. Cold-formed sections have experienced pronounced plastic deformation, the extracted coupon exceedingly curved after removal from the section due to the release of the bending residual stresses through the thickness. No attempt was made to strengthen the coupon prior to tensile testing [31, 67]. The comparison of stress-strain curves for the flat and corner coupons are depicted in Fig. 10. In Fig.10, the strength enhancement due to press-braking fabrication can be clearly observed. Similarly, the tensile tests for coupons extracted at the welding seams of the hollow sections were also carried out following the same procedures as those for corner tensile coupons and the resultant stress-strain curves display softening stiffness with relatively higher ultimate strength but lower yield strength compared with those of flat and corner coupons.

3.3 Quarter-section and half-section coupons

From the comparisons of the respective stress-strain curves of the flat and corner coupons, the underlying different material properties have amply elucidated the heterogeneous mechanical characteristics affected by manufacturing processes. Thus, to better understand the impact of fabrication processes on the variation of the material properties within the section, numerous coupons named as “quarter-section coupons” and “half-section coupons” were machined from the cold-formed HSS IHexHS by assuming that the distribution of the material properties was symmetrically distributed owing to the dual symmetric geometric dimensions and fabrication. Moreover, the coupon at the welding bead is also extracted to examine any effect within the HAZ. The remaining coupons were taken subsequently within the section in the flat or corner portion including two corner coupons with angle equal to 90 degrees and 135 degrees to investigate the variation of the material properties. The locations for the specimens across different HSS cold-formed IHexHS are depicted in Figs. 11–14. The distribution and the magnitude of the yield strength and ultimate strength measured for the coupons within the sections are plotted against the corresponded extracted locations with labeling, as shown in Figs. 11–14. The measured material properties are also summarized in Tables 8–11.

It should be noted that the coupons taken from the corner with 90 degrees curved more severely than the ones taken from 135 degrees corner, which can be primarily attributed to the relatively higher level of strain hardening and plastic deformation, indicating that the underlying cold-forming effect on the enhancement of the material properties was proportionally dependent on the angle of the cold-formed sections subjected to press-braking. Therefore, the strength enhancement at corner regions would be discussed in the following sections. Typical failure modes of the coupons within the sections for the section of CF2-200 × 6-2.00 are depicted in Fig. 9. The graphs of strength distribution within the sections demonstrate the variation of the material properties largely depending on the fabrication methods. The yield strength and ultimate strength at the corner regions generally improved significantly more than the coupons taken from the flat portions. The variation patterns of the material properties for IHexHS CF2-series generally exhibit similar characteristics and the yield strength of the welding coupon is lower than the coupon from the flat and corner portion due to the softening modulus.

Compared with the average yield strength of the parent plates, strength enhancement of 2.3%, 2.4% based on averaged yield strength of flat coupons from sections of CF1-145 × 6-1.75, CF2-145×6-1.75 has been observed while negligible improvement has been observed for flat coupons of CF2-220×6-2.00 and CF2-145×10-1.75 sections respectively. An increased value of 1.3%, 1.9% and 0.6% was observed for ultimate strength of sections of CF1-145 × 6-1.75, CF2-145 × 6-1.75 and CF2-145 × 10-1.75 compared with the averaged ultimate strength from parent plate, the improvement of ultimate strength for flat coupons adjacent the corners from section of CF2-220 × 6-2.00 is quite limited. The strength for the corner coupons in terms of the yield strength in comparison with that of flat coupons was improved by 8.8%, 9.5% 5.2% and 1.9% on average and the ultimate strength increased with 8.3%, 9.2%, 5.2% and 3.4% respectively for sections of CF1-145 × 6-1.75, CF2-145 × 6-1.75, CF2-220 × 6-2.00, CF2-145 × 10-1.75.

The obtained test results were also compared with the requirements given by EN 1993-1-1 [71], EN 1993-1-12 [41], UK National Annex to EN 1993-1-1 [72] and UK National Annex to EN 1993-1-12 [73]. For example, the ratio of the ultimate strength to the yield strength should be greater than 1.10 with elongation strain at failure greater than 15% and 15 times the yield strain for the steels with nominal values of the steel grade up to 460 MPa, as specified in EN 1993-1-1 [71]. The requirement is more stringent in the UK National Annex for plastic design which requires the ratio of ultimate strength to yield strength no less than 1.15, and the fracture strain should be no less than 20 times the yield strain. For the design of high strength steel, EN 1993-1-12 [73] lowers the requirement on the strength ratio to 1.05 whereas UK National Annex specified the ratio should be at least 1.10. For elongation, both UK National Annex [72,73] and EN 1993-1-12 [73] specify 10% elongation should be met for HSS materials. Reduced elongations are observed for corner coupons compared that for flat coupons,due to the press-braking fabrication, as shown in Fig. 17. As seen in Fig. 15, all types of the coupons demonstrate that the properties meet the requirements of the strength ratio specified by EN 1993-1-1 [71]. In terms of the strain at failure, corner coupons cannot meet the requirements from both Eurocode and the UK National Annex due to the reduced ductility caused by press-braking, as shown in Fig. 16. All the coupons can fulfill the elongation requirement, as depicted in Fig. 17.

3.4 Strength enhancements at corner region

The strength enhancements were observed from the coupons taken from the corner regions from the cold-formed hollow sections. In particular, the enhancement is proportionally related to the angle of the cold-formed sections under press-braking. Hence, appropriate models to predict the enhancements of the material properties at corner regions with different angles are indispensable for the purpose of accurate design. Different models proposed for predicting the corner strength enhancements are assessed and compared. The model to predict the increased strength was firstly proposed by Karren [68] and subsequently adopted in international design specification for the Design of Cold-formed Steel Structural Members, AISI S100-16 [74], as given in Eqs. (1) – (3),

$$f_{\mathrm{y,c}} = \frac{B_{\mathrm{c}}}{(r_{\mathrm{i}}/t)^{\alpha}} f_{\mathrm{y}} \tag{1}$$

Where

$$B_{\mathrm{c}} = 3.69\left(\frac{f_{\mathrm{u}}}{f_{\mathrm{y}}}\right) - 0.819\left(\frac{f_{\mathrm{u}}}{f_{\mathrm{y}}}\right)^2 - 1.79 \tag{2}$$

$$\alpha = 0.192(\frac{f_{\mathrm{u}}}{f_{\mathrm{y}}})\text{-}0.068 \tag{3}$$

where f_{u} indicates the ultimate strength of the steel plate, f_{y} is the yield strength of the steel sheet, r_{i} is the inner corner radius, t is the thickness of the steel plate.

Nevertheless, the suitability of the predictive equations for HSS IHexHS was unknown and it is assessed based on the material properties obtained in this study. In addition, Pham et al. [69] have proposed the prediction models for G450 cold-formed steel channels with nominal yield strength of 450 MPa. The form of the prediction formulae stems from the design equations giving by Karren [68] by revising the magnitude of coefficients, as given in Eqs. (4) – (5). The applicability of the Eqs. (4) and (5) to the strength enhancement of Q690 corner with 90 degrees is also assessed.

$$B_{\mathrm{c}} = 1.588(\frac{f_{\mathrm{u}}}{f_{\mathrm{y}}}) - 0.218(\frac{f_{\mathrm{u}}}{f_{\mathrm{y}}})^2 - 0.038 \tag{4}$$

$$\alpha = 0.228(\frac{f_{\mathrm{u}}}{f_{\mathrm{y}}}) - 0.068 \tag{5}$$

Moreover, Gardner et al. [70] modified the predictions for the corner tensile coupons accounting for the adjacent region effect by revising the equations for coefficients, as given below in Eqs. (6) – (7),

$$B_{\mathrm{c}} = 2.9(\frac{f_{\mathrm{u}}}{f_{\mathrm{y}}}) - 0.752(\frac{f_{\mathrm{u}}}{f_{\mathrm{y}}})^2 - 1.09 \tag{6}$$

$$\alpha = 0.23(\frac{f_{\mathrm{u}}}{f_{\mathrm{y}}}) - 0.011 \tag{7}$$

Although the effect of cold-forming process on the material strength was also accounted by Chinese design standard of cold-formed thin-wall structures GB 50018-2002 [75] and European standard EN 1993-1-3 [76], the design equation does not account for other cross sections other than square sections, thus it is not assessed for HSS cold-formed IHexHS. The measured material properties for corner coupons were compared with the predicted values using these respective methods and are tabulated in Table 11. The predicted method from Karren [68] generates the most accurate predictions in comparison with the other two methods. It should be noted that corner coupons with 90 degrees generally exhibit higher yield strength than the corner coupons extracted from the portion with 135 degrees. The yield strength and ultimate strength of corner coupon of CF1-145 × 6-1.75-C7 is 2.3% and 2.6% higher than that of CF1-145 × 6-1.75-C5. The yield strength and ultimate strength of CF2-145 × 10-1.75-C7 is 1.4% and 2.4% than that of CF2-145 × 10-1.75-C4, indicating that the increased level of strength enhancement is principally proportional to the strain hardening level induced by the different angle of press-braking. Although the proposed three methods can provide comparable predictions, the effect of the press-braking angle should be taken into consideration for further investigations.

3.5 DIC measurement

Apart from the tensile coupon tests carried out to investigate the variations of the material properties, four tensile coupons were prepared for conducting digital image correlation (DIC) measurements. By using DIC, the full strain fields along the gauge length during the complete tensile testing process can be obtained beyond the pre-necking stage to generate supplementary strain data to overcome the limitation of strain gauge or extensometer measurements after the occurrence of diffuse necking. The dimensions of the four tensile coupons of CF2-145 × 6-1.75-F2D, CF2-145 × 6-1.75-F4D, CF2-145 × 10-1.75-F3D and CF2-145 × 10-1.75-F6D respectively, with D representing the specimens for DIC measurements, were measured prior to the tensile test. The four tensile coupons were extracted from the sections by wire-cutting method. These four tensile coupons were labelled similar to the tensile coupon in previous sections. For instance, the tensile coupons of CF2-145 × 6-1.75-F2D was machined from the other half-section of CF2-145 × 6-1.75 at a location same as the tensile coupon of CF2-145 × 6-1.75-F2. The symbols of the tensile coupons for DIC measurement are shown in Fig. 18 and the dimensions are summarized in Table 12.

To enable the DIC measurements, random speckle patterns were sprayed on the surface of the tensile coupons while the scheme of the measuring process is described in Fig. 18. After completion of the DIC measurements, deformations and strain distributions recorded using DIC methods corresponding to various stages of yielding, onset of diffuse necking, diffuse necking I and diffuse necking II and localized necking are analyzed and depicted in Fig. 19. In terms of the post necking stage, stages of diffuse necking I and diffuse necking II were defined as the strength decreased to 1% and 5% of ultimate strength. It is apparent that the strain distribution is generally uniformly distributed along the gauge length during the yielding stage with true strain equal to 0.6% and engineering strain at about 0.6%. The diffused necking occurs when the true strain was reaching at about 8.5% after which the strains become severely localized in the vicinity of the cross section where necking mobilized. Maximum true strains for the tensile coupons of Q690 steel can reach up to 89% to 92% with engineering strain reaching at 16.5% to 16.9% for 6 mm and 10 mm thick tensile coupons.

The detailed measurement results are presented in Table 13. The distribution of the longitudinal strain along the gauge length for the coupon of CF2-145 × 6-1.75-CF2-D is plotted in Fig. 24 to illustrate the variation of the strain distribution during different deformation stages under large displacements. Before the process of onset of the diffuse necking, the strains remain uniformed distributed along the gauge length. Significant strain variations appear when the true strain is reaching up to 32% with engineering strain at about 8.6%.

4 Material models

With the development of the finite element modelling techniques, the commercial finite element packages, such as ABAQUS and ANSYS can accurately predict the structural behaviour of steel elements undergo large strain and deformations. Hence, accurate and appropriate material models are of vital importance to the replication of material properties for structural analysis. Different stress-strain curve patterns have been observed for hot-rolled or cold-formed steel structures due to different influences of fabrication processes.

The model developed by Yun and Gardner [77] for hot-rolled steel can be used to develop stress-strain curves with yield plateau. The Ramberg-Osgood relationship is widely adopted as the basic form in developing the full range stress-strain relationship for cold-formed steel sections [78,79]. Therefore, the characteristics and suitability of these stress-strain models for hot-rolled and cold-formed steel are briefly introduced and discussed. A new model which can precisely describe the development of the stress-strain curves for the materials at flat and corner portions in HSS cold-formed IHexHS was proposed.

4.1 Stress-strain models for hot-rolled steel

Hot-rolled steel is generally accompanied by a sharply defined yield point following the linear elastic range. After the yielding stage, pronounced strain hardening occur associated with moderate development of the strain. To better predict the hot-rolled steel behaviour and overcome the unduly under-estimated the stress from EN 1993-1-1 [71] and ANSI/AISC 360-10 [42] which assumes a constant yield strength without consideration of strain hardening, efforts have been consistently made to address these inaccurate predictions and improve the accuracy of stress-strain curve estimation. To avert overly-conservative prediction or unduly neglect of stiffness increasing, particular focus was paid on the strain hardening stage. Quad-linear material model was proposed by Boeraeve et al. [80] and further revised by Yun and Gardner [77]. To trace the gradual loss of the stiffness, power model was proposed, as shown in Eq. (8),

$$\sigma = \begin{cases} E_s \varepsilon & \text{for } \varepsilon \le \varepsilon_y \\ f_y & \text{for } \varepsilon_y \le \varepsilon \le \varepsilon_{sh} \\ f_y + (f_u - f_y)[0.4\varepsilon_x + 2\varepsilon_x / (1 + 400\varepsilon_x{}^5)^{\frac{1}{5}}] & \text{for } \varepsilon_{sh} \le \varepsilon \le \varepsilon_u \end{cases} \tag{8}$$

where ε_x is equal to $(\varepsilon-\varepsilon_{sh})/(\varepsilon_u-\varepsilon_{sh})$ and E_s is the elastic modulus of steel. It should be noted that hardening strain ε_{sh} generally is not provided in the mill certificates and it is obtained from the empirical equation derived on the basis of the regression analysis as following, from Eqs. (9) – (10)

$$\varepsilon_{sh} = 0.1\frac{f_y}{f_u} - 0.055 \qquad \text{for } 0.015 \le \varepsilon_{sh} \le 0.03 \tag{9}$$

$$\varepsilon_u = 0.6(1 - \frac{f_y}{f_u}) \qquad \text{for } \varepsilon_{sh} \ge 0.06 \tag{10}$$

It is observed that the some of the stress-strain curves are featured with a moderate level of strain hardening. The stress-strain curve in the non-linear strain hardening range is similar to that of initial part of Ramberg-Osgood model up to 0.2% proof strength. A modified Ramberg-Osgood model to describe the non-linear strain-hardening range is proposed for Q690 HSS IHexHS with the origin of the strain hardening range taken as the point of (ε_{sh}, f_y). The modified R-O relationship was expressed by Eq. (11),

$$\varepsilon^* = \frac{\sigma^*}{E_\mathrm{s}} + \varepsilon_\mathrm{p}^*(\frac{\sigma^*}{f_\mathrm{u}^*})^m \tag{11}$$

where $\varepsilon^*=\varepsilon - \varepsilon_\mathrm{sh}$, $\sigma^*= \sigma - f_\mathrm{y}$, $f_\mathrm{u}^*=f_\mathrm{u} - f_\mathrm{y}$, $E^*= E_\mathrm{sh}$, $\varepsilon_\mathrm{p}^*= \varepsilon_\mathrm{u} - \varepsilon_\mathrm{sh} – (\sigma - f_\mathrm{y})/E_\mathrm{sh}$.

After substiuting the corresponding parameters, the stress-strain relationship can be expressed as Eq. (12)

$$\varepsilon - \varepsilon_\mathrm{sh} = \frac{\sigma - f_\mathrm{y}}{E_\mathrm{sh}} + \left(\varepsilon_\mathrm{u} - \varepsilon_\mathrm{sh} - \frac{f_\mathrm{u} - f_\mathrm{y}}{E_\mathrm{sh}}\right)\left(\frac{\sigma - f_\mathrm{y}}{f_\mathrm{u} - f_\mathrm{y}}\right)^m \tag{12}$$

$$\begin{cases} \text{Bilinear: } \sigma = \begin{cases} E_\mathrm{s}\varepsilon & \text{for } \varepsilon \le \varepsilon_\mathrm{y} \\ f_\mathrm{y} & \text{for } \varepsilon_\mathrm{y} < \varepsilon \le \varepsilon_\mathrm{sh} \end{cases} \\ \text{nonlinear: } \varepsilon = \varepsilon_\mathrm{sh} + \dfrac{\sigma - f_\mathrm{y}}{E_\mathrm{sh}} + \left(\varepsilon_\mathrm{u} - \varepsilon_\mathrm{sh} - \dfrac{f_\mathrm{u} - f_\mathrm{y}}{E_\mathrm{sh}}\right)\left(\dfrac{\sigma - f_\mathrm{y}}{f_\mathrm{u} - f_\mathrm{y}}\right)^m \quad \text{for } \sigma > f_\mathrm{y} \end{cases} \tag{13}$$

where m is the strain-hardening exponent, E_sh is the initial slope of the stress-strain curves in the strain-hardening range, also termed as hardening modulus. E_sh can be directly obtained from material tests. If the value of E_sh is not reported, Eq. (14) proposed in Yun and Gardner [77] might be used to determine the value.

$$E_\mathrm{sh} = \frac{f_\mathrm{u} - f_\mathrm{y}}{0.4(\varepsilon_\mathrm{u} - \varepsilon_\mathrm{sh})} \tag{14}$$

Compared with the non-linear strain-hardnening range between the experimental data and the material models proposed by Yun and Gardner [77], it was found that Yun and Gardner's model unduly overestimate the strain-hardening response that the strain predicted from Yun and Gardner's model is comparatively larger than that from experimental measurements, as shown in Figs. 20(a)–(b). Expressions for the required parameters ε_u and ε_sh are proposed here after collating the database based on Q690 steel which can be obtained based on expressions in Eqs. (15) – (17). Compared with the predictions from the Yun and Gardner [77], the proposed method can trace the experimental curve well in the stage of strain hardening, see Fig. 20(a) for flat coupons taken from CF2-145 × 6-1.75-F2 and Fig. 20(b) for flat coupon from the section of CF2-145 × 10-1.75-F3. Thus, it is recommended to employ the proposed method in predicting the stress-strain curve of Q690 steel with yield plateau for second strain hardening range.

$$\varepsilon_\mathrm{sh} = \text{-}0.04\frac{f_\mathrm{y}}{f_\mathrm{u}} + 0.06 \quad \text{for} \quad 0.01 \le \varepsilon_\mathrm{sh} \le 0.04 \tag{15}$$

$$\varepsilon_{\mathrm{u}} = 0.55(1-\frac{f_{\mathrm{y}}}{f_{\mathrm{u}}})+0.03 \tag{16}$$

$$m = 1+3.3(\frac{f_{\mathrm{y}}}{f_{\mathrm{u}}}) \tag{17}$$

4.2 Stress-strain model for cold-formed steel

Cold-formed steel sections can undergo severe plastic deformation which results in a relatively rounded response of the stress-strain behaviour compared with that of hot-rolled steel, especially for the cold-bent corner with smaller corner radius thickness ratio. The Ramberg-Osgood relationship [81,82] as shown in Eq. (18) is employed as the basic form to construct the stress-strain curve of cold-formed stainless steels. Based on two-stage form of the equation, Gardner and Yun [79] proposed a two-stage stress-strain model for cold-formed carbon steel, which is applicable to the cold-formed carbon steel and steel sheets with yield strength up to 900 MPa.

$$\varepsilon = \frac{\sigma}{E_{\mathrm{s}}} + 0.002(\frac{\sigma}{f_{\mathrm{y}}})^{n} \tag{18}$$

To accurately represent the curve up to the ultimate strength without overly predict the yield strength, Gardner and Yun [79] extensively collected stress-strain curves aiming at developing material models applicable for cold-formed carbon steel precisely with expressions given as follows,

$$\varepsilon = \begin{cases} \dfrac{\sigma}{E_{\mathrm{s}}} + 0.002\left(\dfrac{\sigma}{f_{0.2}}\right)^{n} & \text{for } \sigma \le f_{0.2} \\ \dfrac{\sigma - f_{0.2}}{E_{0.2}} + \left(\varepsilon_{\mathrm{u}} - \varepsilon_{0.2} - \dfrac{f_{\mathrm{u}} - f_{0.2}}{E_{0.2}}\right)\left(\dfrac{\sigma - f_{0.2}}{f_{\mathrm{u}} - f_{0.2}}\right)^{m} + \varepsilon_{0.2} & \text{for } \sigma > f_{0.2} \end{cases} \tag{19}$$

$$E_{0.2} = \frac{E_{\mathrm{s}}}{1+0.002nE_{\mathrm{s}} / f_{0.2}} \tag{20}$$

or alternatively obtained from the following with the proof 1.0% stress needed,

$$m=\frac{\ln(0.008+\dfrac{f_{1.0}-f_y}{E}-\dfrac{f_{1.0}-f_y}{E_{0.2}})-\ln(\varepsilon_{\mathrm{u}}-\varepsilon_{0.2}-\dfrac{f_{\mathrm{u}}-f_{\mathrm{y}}}{E_{0.2}})}{\ln(f_{1.0}-f_{\mathrm{y}})-\ln(f_{\mathrm{u}}-f_{\mathrm{y}})} \tag{21}$$

Rasmussen and Hancock [78], Gardner and Yun [79], and Arrayago et al. [83] concluded that with the use of 0.05% proof stress instead of 0.01% proof stress in the model yields more consistent values. Thus, the first stage hardening component *n* is determined as following,

$$n=\frac{\ln(4)}{\ln(f_{\mathrm{y}}\,/\,f_{0.05})} \tag{22}$$

Material model concerning with HSS is proposed by Ma et al. [2] by relating the strain hardening component to plastic strain ε_{p}, by which the strain hardening component can be obtained based on the Eq. (23),

$$n_{\mathrm{pro}}=f(\varepsilon_{\mathrm{p}})=n+K\varepsilon_{\mathrm{p}}{}^{m} \tag{23}$$

m and *K* are the coefficient used to determine the proportionally increased strain hardening exponent n_{pro}. Coefficient *K* is determined based on the Eq. (24) as below,

$$K=[\log_{\frac{f_{\mathrm{u}}}{f_{0.2}}}(\frac{\varepsilon_{\mathrm{u}}-f_{\mathrm{u}}\,/\,E_{\mathrm{s}}}{0.002})]\,/\,(\varepsilon_{\mathrm{u}}-f_{\mathrm{u}}\,/\,E_{\mathrm{s}})^{m} \tag{24}$$

$$\varepsilon_{\mathrm{p}}=\varepsilon-\frac{\sigma}{E_{\mathrm{s}}}=0.002(\frac{\sigma}{f_{0.2}})^{n_{\mathrm{pro}}} \tag{25}$$

Substituting Eq. (24) and Eq. (25) into Eq. (23), the expression of Eq. (26) can be obtained as following, by which the predicted strength and the stress-strain correlated well with the experimental stress-strain curve.

$$\begin{cases}\sigma=\left(\dfrac{\varepsilon_{\mathrm{p}}}{0.002}\right)^{\left(\frac{1}{n+K\varepsilon_{\mathrm{p}}^{m}}\right)}f_{0.2}\\[2ex] \varepsilon=\varepsilon_{\mathrm{p}}+\dfrac{\sigma}{E_{\mathrm{s}}}=\varepsilon_{\mathrm{p}}+\dfrac{f_{0.2}}{E_{\mathrm{s}}}\left(\dfrac{\varepsilon_{\mathrm{p}}}{0.002}\right)^{\left(\frac{1}{n+K\varepsilon_{\mathrm{p}}^{m}}\right)}\end{cases} \tag{26}$$

Likewise, the predictive material model for HSS Q690 cold-formed octagonal hollow sections has also been studied and proposed by Fang et al. [33], see Eqs. (27) – (29). The accuracy of the model was subsequently assessed against the experiment data for flat coupon and the corner coupon with 135 degrees.

$$\varepsilon=\begin{cases}\dfrac{\sigma}{E_{\mathrm{s}}}+0.002(\dfrac{\sigma}{f_{0.2}})^{n} & \text{for } \sigma\leq f_{0.2}\\ \dfrac{\sigma\text{-}f_{0.2}}{E_{0.2}}+(\varepsilon_{\mathrm{u}}-\varepsilon_{0.2}-\dfrac{f_{\mathrm{u}}-f_{0.2}}{E_{0.2}})(\dfrac{\sigma-f_{0.2}}{f_{\mathrm{u}}-f_{0.2}})^{\mathrm{m}}+\varepsilon_{0.2} & \text{for } \sigma\geq f_{0.2}\end{cases} \tag{27}$$

where,

$$n=\begin{cases}\dfrac{\ln(0.2/0.01)}{\ln(f_{0.2}/f_{0.01})}+\log_{\frac{f_{\mathrm{u}}}{f_{0.2}}}(\varepsilon_{\mathrm{u}}/0.002) & \text{for flat portion}\\ \dfrac{\ln(0.2/0.01)}{\ln(f_{0.2}/f_{0.01})} & \text{for corner portion}\end{cases} \tag{28}$$

$$m=\frac{\ln(\varepsilon_{\mathrm{u}}/\varepsilon_{0.2})}{\ln(f_{\mathrm{u}}/f_{0.2})} \tag{29}$$

Based on the comparisons between the curves of experimental test data and the predictions from previous researchers for the stress-strain curves with rounded response, the method recommended from Gardner and Yun [79] and Fang et al. [33] can generally capture the hardening path of the stress-strain curves. The predictions from Gardner and Yun [79] can generate more accurate data close to the test results than the later one, as shown in Fig. 21(a) and Fig. 21(c). However, both methods cannot trace the gradually decreased stiffness of the curve in the second hardening stage, as shown in Fig. 21(b) and Fig. 21(d). Thus, a new method which can more accurately trace the gradually increasing angle of the curve in second stage is proposed. In the proposed method, the stress-strain relationship in the second stage can be described by adding the component with yield stress shown in Eq. (30). The factor of K^* and m^* are utilized to describe the strain hardening level and the relationship between the stress and strain in the second hardening stage can be transformed into logarithmic function, and then the stress strain relationship can be correlated as linear relationship, which can be derived based on Eqs. (32) – (33). It should be noted that in Eq. (33), in determination of the strain hardening component m^*, the strain at 0.5% proof stress is utilized. In Eq. (30), E_{h} is the exponential coefficient to construct the stress-strain relationship, which can be obtained as the intercept of the ordinate after linear transformation and n^* is the slope of the linear transformation. Then the obtained coefficient is subsequently compared with the ratio between K^* and m^*. Subsequently, the iteration process was performed based on the comparison between the predicted curve and the experimental result until the comparison provides a good agreement with iterated E_{h}^* by fitting the curve to the tested stress-strain curve data.

$$\sigma=\sigma_y+\mathrm{e}^{E_{\mathrm{h}}}\,\varepsilon^{n^*} \tag{30}$$

$$E_{\mathrm{sh}}{}^*=\frac{K^*}{m^*} \tag{31}$$

$$K^{*} = \log_{\frac{\sigma_{\mathrm{u}}}{\sigma_{0.2}}}\left(\frac{\varepsilon_{\mathrm{u}}}{0.002}\right) \tag{32}$$

$$m^{*} = \frac{\ln(\varepsilon_{\mathrm{u}} / \varepsilon_{0.5})}{\ln(f_{\mathrm{u}} / f_{0.5})} \tag{33}$$

5 Residual stresses investigation

Residual stresses can adversely affect the behaviour of cold-formed steel structures. Premature yielding through part of the material thickness led to further loss of the stiffness of the structure due to the superimposed stresses, invariably resulting in the instability and subsequent reductions of the resistance of the structural members [84]. The residual stresses measurements in this study focused on those in the longitudinal direction, as suggested in [85–87] that residual stresses in longitudinal directions are more influential than those in the transverse direction. The residual stresses can be de-composed into membrane residual stresses and bending residual stresses. Membrane residual stresses are more dominant in hot-rolled steel section or built-up sections caused by welding, generated from uneven cooling, heating, etc. whereas bending residual stresses are primarily encountered in cold-formed sections [6] due to the process of (i) press-braking (ii) cold-rolled process (iii) Coiling and uncoiling of the steel sheet, etc. assuming that the stresses varied linearly through the thickness of the steel plate [84], as presented in Fig. 22. There is a variety of techniques for residual stress measurements and the techniques can mainly be classified as destructive methods and non-destructive methods. Destructive methods are generally referred to the sectioning and hole-drilling method, whereas non-destructive methods include X-ray diffraction method, neutron or electron diffraction method, ultrasonic method and magnetic methods. Sectioning method is a popular destructive method based on measuring the deformations of the material when extracted from the structural members and has been successfully applied by numerous researchers [32,33,88]. Therefore, the sectioning method was adopted in this study.

5.1 Measurement of the residual stresses

The specimens of CF1-145 × 6-1.75, CF2-145 × 6-1.75, CF2-220 × 6-2.00 and CF2-145 × 10-1.75 were investigated for residual stresses distribution and magnitudes. The length of specimens used in this study is 400 mm. The specimen lengths are long enough to minimize the possibility that the operation of cutting may disturb the residual stress pattern in the centre portion of the specimen [87]. Due to the symmetrical geometry dimension, half section of CF1-145 × 6-1.75 and quarter sections of the remainders were marked into longitudinal strips with width varying between 10 mm, 12 mm and 15 mm depending on the residual stress gradient and distribution. Strain gauges of model FLAB-5-11-1LJC-F from Tokyo Sokki Kenkyujo with a 5 mm gauge length were used to obtain reliable and accurate measurements of strains up to 5%. Strain gauges were attached to the outer and inner surfaces of the marked longitudinal strips at mid-height of each strip with waterproof tape carefully coating each electrical strain to avoid any damage during the cutting process. A typical specimen with the external and internal gauges as CF2-220 × 6-2.00 is presented in Fig. 23.

Both the initial readings from external and internal strain gauges were taken prior to the process of sectioning. The wire cutting method was subsequently employed to perform the sectioning with coolant sprayed to minimize the heat generated during the sectioning, as shown in Fig. 24. After the completion of the sectioning process, the released residual stresses induced by manufacturing processes were obtained from the strain gauges readings. For each strain gauge, readings measured for at least three times were recorded and the mean value was used for subsequent analysis. The residual strains on the outer and inner surfaces of each longitudinal strip were measured based on the differences between the strains before and after the sectioning process. By subtracting the initial strain readings from the final readings, the residual strains can be determined. Moreover, the membrane and bending residual strain can be determined from Eq. (35) and Eq. (36) after which the residual stresses can be derived on the basis of the simple Hook's Law. It should be noted that positive and negative values indicate tensile and compression residual stresses respectively.

$$\sigma_m = -\left(\frac{\varepsilon_{\text{ext}} + \varepsilon_{\text{int}}}{2}\right)E_s = -\left(\frac{\varepsilon_{\text{ext,f}} - \varepsilon_{\text{ext,i}}}{2} + \frac{\varepsilon_{\text{int,f}} - \varepsilon_{\text{int,i}}}{2}\right)E_s \tag{35}$$

$$\sigma_b = -\left(\frac{\varepsilon_{\text{ext}} - \varepsilon_{\text{int}}}{2}\right)E_s = -\left(\frac{\varepsilon_{\text{ext,f}} - \varepsilon_{\text{ext,i}}}{2} - \frac{\varepsilon_{\text{int,f}} - \varepsilon_{\text{int,i}}}{2}\right)E_s \tag{36}$$

where E_s is the elastic modulus of steel, ε_{ext} is the difference between the initial strain readings $\varepsilon_{\text{ext,i}}$ and the final readings $\varepsilon_{\text{ext,f}}$ after wire-cutting for external strain gauge, ε_{int} is the the difference between the initial readings $\varepsilon_{\text{int,i}}$ and the final readings $\varepsilon_{\text{int,f}}$ after wire-cutting for internal strain gauge.

5.2 Results and discussion

The extracted strips from the press-braked sections deformed with larger curvatures as result of the large bending residual stresses. The deformed strips after cutting from the specimen CF2-220 × 6-2.00 can be seen in Fig. 25. The strips from the corner portion with the angle of 90° curved more severely than their counterpart with the angle of 135° due to the associated excessively strain hardening and pronounced plastic deformation experienced during press-braking process. This observation indicates that the bending residual stresses are much larger at the corner than any other regions, particularly for the tip two corners with 90 degrees.

Magnitude and the distribution of the longitudinal residual stresses in HSS cold-formed irregular hexagonal sections CF1-145 × 6-1.75, CF2-145 × 6-1.75, CF2-220 × 6-2.00 and CF2-145 × 10-1.75 were determined. The obtained residual stresses were normalized to the yield strength of parent plate and plotted with respect to the distance from the welding seam.

The normalized membrane and bending residual stresses of these four sections can be seen in the Figs. 26–29. The maximum tensile bending residual stresses in CF1-145 × 6-1.75, CF2-145 × 6-1.75, CF2-220 × 6-2.00 and CF2-145 × 10-1.75 sections respectively were 39%, 35%, 39% and 36% of the $f_{0.2,\text{p}}$ of the parent plate. In terms of membrane residual stresses, maximum tensile membrane residual stresses were found at the welding seam and became relatively small at other regions. The maximum membrane residual stresses were larger than the bending residual stresses. It is found that the maximum membrane residual stresses for CF1-145 × 6-1.75, CF2-145 × 6-1.75, CF2-220 × 6-2.00 and CF2-145 × 10-1.75 were 53, 52, 50 and 52% of the $f_{0.2,\,p}$ of the parent plate. The ratio of width to thickness has negligible effect on the residual stress magnitudes and distributions based on the obtained test results. After comprehensively compare the magnitude and distribution of the membrane and residual stresses for sections of CF1-145 × 6-1.75 and CF2-145 × 6-1.75, the different patterns existed in these two sections further demonstrate the effect of the fabrication route on residual stresses should be accounted for in the analysis.

5.3 Predictive model for residual stress

The predictive models for residual stresses magnitudes and distribution are developed based on the results described in Section 6.2 and can be applicable for accurate analysis of structural behaviour of cold-formed HSS irregular hexagonal sections. Multi-linear model was adopted as the simplified method for the ease of application purposes with constant bending residual stresses taken at corners and the constant value at other regions whereas linear and constant relationship for membrane residual stresses is proposed. It should be noticed that the total net force of the outer stresses and the inner stresses should be zero in total. The magnitudes of the residual stresses given in the models were obtained as the average membrane and bending residual stresses over different locations of the hollow sections and the distribution models are plotted with respect to half-section and quarter-sections with normalized values accompanied by parent plate strength $f_{0.2,\,p}$, as depicted in Figs. 30 and 31.

6 Conclusions

The material property variations within the cold-formed high strength steel irregular hexagonal sections have been investigated in this study. Tensile coupon tests were conducted for the specimens extracted from various critical locations. Strength enhancement of 3.5%, 3.5%, 0.8% and 4.5% based on averaged yield strength from sections of CF1-145 × 6-1.75, CF2-145 × 6-1.75, CF2-220 × 6-2.00 and CF2-145 × 10-1.75 have been observed compared with the average yield strength measured for the parent plates. An increment of 2.4%, 3.0%, 1.1% and 3.0% in ultimate strength was observed for those sections compared with the averaged ultimate strength of the respective parent plates. The stress-strain model to describe the material relationship is proposed and validated. The digital image correlation measurement was performed to examine the strain characteristics beyond diffuse necking with large deformations during entire life, maximum true strain for the tensile coupon of the steel from cold-formed high strength steel irregular hexagonal sections can reach up to 89% to 92% with engineering strain reaching at 15.8% to 16.9%. The membrane and bending residual stresses were also measured and plotted along either the half-section or quarter section of the studied sections. The maximum membrane residual stresses are invariably larger than the bending residual stresses. It is found that the maximum membrane residual stresses for CF1-145 × 6-1.75, CF2-145 × 6-1.75, CF2-220 × 6-2.00 and CF2-145 × 10-1.75 were 56, 55, 53 and 55% of the $f_{0.2,\,p}$ while the maximum tensile bending residual stresses in CF1-145 × 6-1.75, CF2-145 × 6-1.75, CF2-220 × 6-2.00 and CF2-145 × 10-1.75 sections respectively were 41, 38, 39 and 42% of the $f_{0.2,\,p}$ of the parent plate. Based on the measured results for residual stresses distribution, predictive models are proposed and can be used for the structural analysis of cold-formed high strength steel irregular hexagonal sections.

Acknowledgements

The research work presented in this paper was supported by a grant from the Research Grants Council of the Hong Kong Special Administrative Region, China (Project no. 152189/18E). The authors would like to sincerely acknowledge the support from the Innovation and Technology Fund - Nano and Advanced Materials Institute (ITF-NAMI) for the project "Hong Kong Modular Integrated Construction (MiC) Innovations" (PolyU/ ZS12) and from the Chinese National Engineering Research Centre for Steel Construction (Hong Kong Branch) at The Hong Kong Polytechnic University. The authors would also like to thank the technical staff, Mr. H.Y. Leung, Mr. K.L. Cheung of the Structural Engineering Research Laboratory for their support as well as the support from the Industrial Center at The Hong Kong Polytechnic University.

References

[1] Chan T−M, Zhao X-L, Young B. Cross-section classification for cold-formed and built-up high strength carbon and stainless steel tubes under compression. J Constr Steel Res. 2015;106:289-95.

[2] Ma J-L, Chan T-M, Young B. Material properties and residual stresses of cold-formed high strength steel hollow sections. J Constr Steel Res. 2015;109:152-65.

[3] Wang J, Afshan S, Schillo N, Theofanous M, Feldmann M, Gardner L. Material properties and compressive local buckling response of high strength steel square and rectangular hollow sections. Eng Struc. 2017;130:297-315.

[4] Chen J, Fang H, Chan T-M. Design of fixed-ended octagonal shaped steel hollow sections in compression. Eng Struc. 2021;228:111520.

[5] Lan X, Chan T-M, Young B. Experimental and numerical studies on stress concentration factors of high strength steel fabricated box X-joints. Thin-Walled Struct. 2021;164:107858.

[6] Chen J, Liu H, Chan T-M. Material properties and residual stresses of cold-formed octagonal hollow sections. J Constr Steel Res. 2020;170:106078.

[7] Yao Y, Quach W-M, Young B. Finite element-based method for residual stresses and plastic strains in cold-formed steel hollow sections. Eng Struc. 2019;188:24-42.

[8] Nishino F, Ueda Y, Tall L. Experimental investigation of the buckling of plates with residual stresses. Test methods for compression members: ASTM International; 1967.

[9] Usami T, Fukumoto Y. Local and overall buckling of welded box columns. J Struct Div. 1982;108:525-42.

[10] Usami T, Fukumoto Y. Welded box compression members. J Struct Eng. 1984;110:2457-70.

[11] Rasmussen KJ, Hancock GJ. Plate slenderness limits for high strength steel sections. J Constr Steel Res. 1992;23:73-96.

[12] Wang Y-B, Li G-Q, Chen S-W. The assessment of residual stresses in welded high strength steel box sections. J Constr Steel Res. 2012;76:93-9.

[13] Ban H, Shi G, Shi Y, Wang Y. Residual stress of 460 MPa high strength steel welded box section: Experimental investigation and modeling. Thin-Walled Struct. 2013;64:73-82.

[14] Sun M, Packer JA. Direct-formed and continuous-formed rectangular hollow sections—Comparison of static properties. J Constr Steel Res. 2014;92:67-78.

[15] Kim D-K, Lee C-H, Han K-H, Kim J-H, Lee S-E, Sim H-B. Strength and residual stress evaluation of stub columns fabricated from 800MPa high-strength steel. J Constr Steel Res. 2014;102:111-20.

[16] Somodi B, Kövesdi B. Residual stress measurements on welded square box sections using steel grades of S235–S960. Thin-Walled Struct. 2018;123:142-54.

[17] Khan M, Paradowska A, Uy B, Mashiri F, Tao Z. Residual stresses in high strength steel welded box

sections. J Constr Steel Res. 2016;116:55-64.

[18] Ma J-L, Chan T-M, Young B. Experimental Investigation on Stub-Column Behavior of Cold-Formed High-Strength Steel Tubular Sections. J Struct Eng. 2016;142:04015174.

[19] Chen J, Chan T-M. Material properties and residual stresses of cold-formed high-strength-steel circular hollow sections. J Constr Steel Res. 2020;170:106099.

[20] Chen J, Chan T-M, Varma AH. Stub Column Behavior of Cold-Formed High-Strength Steel Circular Hollow Sections under Compression. J Struct Eng. 2020;146:04020277.

[21] Ma J-L, Chan T-M, Young B. Cold-formed high strength steel tubular beam-columns. Eng Struc. 2021;230:111618.

[22] Yao Y, Quach W-M, Young B. Simplified models for residual stresses and equivalent plastic strains in cold-formed steel elliptical hollow sections. Thin-Walled Struct. 2020;154:106835.

[23]Yao Y, Quach W-M, Young B. Cross-section behavior of cold-formed steel elliptical hollow sections–A numerical study. Eng Struc. 2019;201:109797.

[24] Fang H, Chan T-M, Young B. Behavior of Octagonal High-Strength Steel Tubular Stub Columns. J Struct Eng. 2019;145.

[25] Fang H, Chan T-M, Young B. Experimental and Numerical Investigations of Octagonal High-Strength Steel Tubular Stub Columns under Combined Compression and Bending. J Struct Eng. 2021;147:04020282.

[26] Fang H, Chan T-M, Young B. Structural performance of concrete-filled cold-formed high-strength steel octagonal tubular stub columns. Eng Struc. 2021;239:112360.

[27] Chen J, Zhu J-Y, Chan T-M. Experimental and numerical investigation on stub column behaviour of cold-formed octagonal hollow sections. Eng Struc. 2020;214:110669.

[28] Chen J, Chan T-M. Compressive behaviour and design of compact to slender octagonal concrete-filled steel tubular stub columns. Thin-Walled Struct. 2021;167:108211.

[29] Liu J-Z. Fang H, Chan T-M. Material properties and residual stresses of high strength steel irregular octagonal hollow sections, J. Constr. Steel. Res. 2022; 107170. (Accepted)

[30] Xu W, Han L-H, Li W. Performance of hexagonal CFST members under axial compression and bending. J Constr Steel Res. 2016;123:162-75.

[31] Liu J-Z, Fang H, Chen S, Chan T-M. Material properties and residual stresses of high strength steel hexagonal hollow sections. J Constr Steel Res. 2022; 190, 107061.

[32] Cruise R, Gardner L. Residual stress analysis of structural stainless steel sections. J Constr Steel Res. 2008;64:352-66.

[33] Fang H, Chan T-M, Young B. Material properties and residual stresses of octagonal high strength steel hollow sections. J Constr Steel Res. 2018;148:479-90.

[34] Quach W, Teng J, Chung KF. Effect of the manufacturing process on the behaviour of press-braked thin-walled steel columns. Eng Struc. 2010;32:3501-15.

[35] Quach W, Teng J, Chung KF. Finite element predictions of residual stresses in press-braked thin-walled steel sections. Eng Struc. 2006;28:1609-19.

[36] Quach W, Teng J, Chung KF. Residual stresses in steel sheets due to coiling and uncoiling: a closed-form analytical solution. Eng Struc. 2004;26:1249-59.

[37] Quach W, Teng J, Chung KF. Residual stresses in press-braked stainless steel sections, I: Coiling and uncoiling of sheets. J Constr Steel Res. 2009;65:1803-15.

[38] Quach W, Teng J, Chung KF. Residual stresses in press-braked stainless steel sections, II: Press-braking operations. J Constr Steel Res. 2009;65:1816-26.

[39] Sefcikova K, Brtnik T, Dolejs J, Keltamaki K, Topilla R. Mechanical properties of heat affected zone of

high strength steels. IOP Conference Series: Materials Science and Engineering: IOP Publishing; 2015. p. 012053.

[40] Liu X, Chung K-F, Ho H-C, Xiao M, Hou Z-X, Nethercot DA. Mechanical behavior of high strength S690-QT steel welded sections with various heat input energy. Eng Struc. 2018;175:245-56.

[41] EN 1993-1-12, Eurocode 3: Design of Steel Structures – Part 1–12: Additional Rules for the Extension of EN 1993 up to Steel Grades S700. Brussels: European Committee for Standardization (CEN); 2007.

[42] ANSI/AISC 360-16, Specification for Structural Steel Buildings. Chicago: American Institute of Steel Construction (AISC); 2016.

[43] EN 10219-2, Cold formed welded steel structural hollow sections. Tolerances, dimensions and sectional properties. Brussels: European Committee for Standardization (CEN); 2019.

[44] GB/T 6728, Cold forming hollow sectional steel for general structure. Beijing, China: Standards Press of China; 2017.

[45] JIS G 3101, Rolled steels for general structure. Japanese Standards Association 2015.

[46] A1085/1085M, Specification for Hollow Structural Sections (HSS). West Conshohocken, PA, USA: American Society for Testing and Materials; 2015.

[47] AWS A5.28/A5.28M, Specification for Low-Alloy Steel Electrodes and Rods for Gas Shielded Arc Welding. United States of America: American Welding Society; 2005.

[48] EN 10025-6, Hot rolled products of structural steels – Part 6: Technical delivery conditions for flat products of high yield strength structural steels in the quenched and tempered condition. Brussels: European Committee for Standardization (CEN); 2004.

[49] GB 50205, Standard for acceptance of construction quality of steel structures. Beijing, China: China Architecture & Building Press; 2020.

[50] GB/T-3323, Non-destructive testing of welds-Radiographic testing - Part 1: X- and gamma -ray techniques with film. Qinhuangdao, China: Standards Press of China; 2019.

[51] ISO 17636-2, Non-destructive testing of welds — Radiographic testing — Part 2: X- and gamma-ray techniques with digital detectors. International Organization for Standardization; 2013.

[52] GB 50661, Code for welding of steel structures. Beijing, China: China Architecture & Building Press; 2011.

[53] A 852/A 852M, Standard Specification for Quenched and Tempered Low-Alloy Structural Steel Plate with 70 ksi [485 MPa] Minimum Yield Strength to 4 in. [100mm] Thick. West Conshohocken, PA, USA: American Society for Testing and Materials; 2007.

[54] ASTM A709/A709M-18: Standard Specification for Structural Steel for Bridges. West Conshohocken, PA, USA: American Society for Testing and Materials; 2018.

[55] EN ISO 6892-1, Metallic Materials – Tensile Testing Part 1: Method of Test at Ambient Temperature. EN ISO 6892-1. Brussels, Belgium: CEN; 2019.

[56] AS 3597, Structural and Pressure Vessel Steel - Quenched and Tempered Plate. Sydney, Australia: Australian Standard; 2008.

[57] GB/T 1591–2008: High Strength Low Alloy Structural Steel. China Standards Press; 2009.

[58] GB/T 19879–2015: Steel Plate for Building Structures. Beijing, China: China Standards Press; 2015.

[59] GB/T 699, Quality carbon structure steels. Bejing, China: Standards Press of China; 2015.

[48] EN 10025-6, Hot rolled products of structural steels – Part 6: Technical delivery conditions for flat products of high yield strength structural steels in the quenched and tempered condition. Brussels: European Committee for Standardization (CEN); 2004.

[60] JIS G 3128: 2009(E): High Yield Strength Steel Plates for Welded Structure. Tokyo, Japan: JSA; 2009.

[61] JIS G 3140: 2011(E): Higher Yield Strength Steel Plates for Bridges. Tokyo, Japan: JSA; 2011.

[62] JIS G 3114, Hot-rolled atmospheric corrosion resisting steels for welded structur. Japanese Standards Association; 2020.

[63] ASTM A1011/A1011M-18a: Standard Specification for Steel, Sheet and Strip, Hot-rolled, Carbon, Structural, High strength Low-alloy, High-Strength Low-alloy with Improved Formability, and Ultra-high Strength. West Conshohocken, PA, USA: American Society for Testing and Materials; 2018.

[64] A 514/A514M , Standard Specification for High-Yield-Strength, Quenched and Tempered Alloy Steel Plate, Suitable for Welding. West Conshohocken: American Society for Testing and Materials; 2019.

[65] A572/572M, Standard Specification for High-Strength Low-Alloy Columbium-Vanadium Structural Steel. West Conshohocken, PA, USA: American Society for Testing and Materials; 2018.

[66] EN 1993-1-8, Eurocode 3: Design of steel structures - Part 1-8: Design of joints Brussels: European Committee for Standardization (CEN); 2005.

[67] Gardner L, Nethercot DA. Experiments on stainless steel hollow sections—Part 1: Material and cross-sectional behaviour. J Constr Steel Res. 2004;60:1291-318.

[68] Karren KW. Corner properties of cold-formed steel shapes. J Struct Div. 1967;93:401-32.

[69] Pham CH, Trinh HN, Proust G. Effect of manufacturing process on microstructures and mechanical properties, and design of cold-formed G450 steel channels. Thin-Walled Struct. 2021;162:107620.

[70] Gardner L, Saari N, Wang F. Comparative experimental study of hot-rolled and cold-formed rectangular hollow sections. Thin-Walled Struct. 2010;48:495-507.

[71] EN 1993-1-1, Eurocode 3: Design of Steel STRUCTURES – Part 1.1: General Rules and Rules for Buildings. Brussels: European Committee for Standardization (CEN); 2005.

[72] National Annex to Eurocode 3: Design of steel structures - Part 1-1: General rules and rules for buildings. UK National Annex to EN 1993-1-1, 2015. BS; 2015.

[73] National Annex to Eurocode 3: Design of steel structures - Part 1-12: Additional rules for the extension of EN 1993 up to steel grades S 700. UK National Annex to EN 1993-1-12, 2008. BS; 2008.

[74] AISI S100-16, North American Specification for the Design of Cold-Formed Steel Structural Members. Washington, DC, USA: AISI (American Iron and Steel Institute); 2016.

[75] GB 50018, Technical code of cold-formed thin-walled steel structures. Beijing, China: China Architecture & Building Press; 2002.

[76] EN 1993-1-3, Eurocode 3: Design of Steel Structures – Part 1–3: General Rules – Supplementary Rules for Cold-Formed Members and Sheeting. Brussels, Belgium: European Committee for Standardization (CEN); 2006.

[77] Yun X, Gardner L. Stress-strain curves for hot-rolled steels. J Constr Steel Res. 2017;133:36-46.

[78] Rasmussen K, Hancock G. Design of cold-formed stainless steel tubular members. II: Beams. J Struct Eng. 1993;119:2368-86.

[79] Gardner L, Yun X. Description of stress-strain curves for cold-formed steels. Constr Build Mater. 2018;189:527-38.

[80] Boeraeve P, Lognard B, Janss J, Gerardy J, Schleich J. Elasto-plastic behaviour of steel frame works. J Constr Steel Res. 1993;27:3-21.

[81] Ramberg W, Osgood WR. Description of stress-strain curves by three parameters. 1943.

[82] Hill H. Determination of stress-strain relations from" offset" yield strength values. ALUMINUM CO OF AMERICA PITTSBURGH PA; 1944.

[83] Arrayago I, Picci F, Mirambell E, Real E. Interaction of bending and axial load for ferritic stainless steel RHS columns. Thin-Walled Struct. 2015;91:96-107.

[84] Gardner L, Cruise R. Modeling of residual stresses in structural stainless steel sections. J Struct Eng. 2009;135:42-53.

[85] Hu Y-F, Chung K-F, Ban H, Nethercot DA. Investigations into residual stresses in S690 cold-formed circular hollow sections due to transverse bending and longitudinal welding. Eng Struc. 2020;219:110911..

[86] Schafer BW, Li Z, Moen CD. Computational modeling of cold-formed steel. Thin-Walled Struct. 2010;48:752-62.

[87] Ziemian RD. Guide to stability design criteria for metal structures: John Wiley & Sons; 2010.

[88] Sun Y, Liang Y, Zhao O. Testing, numerical modelling and design of S690 high strength steel welded I-section stub columns. J Constr Steel Res. 2019;159:521-33.

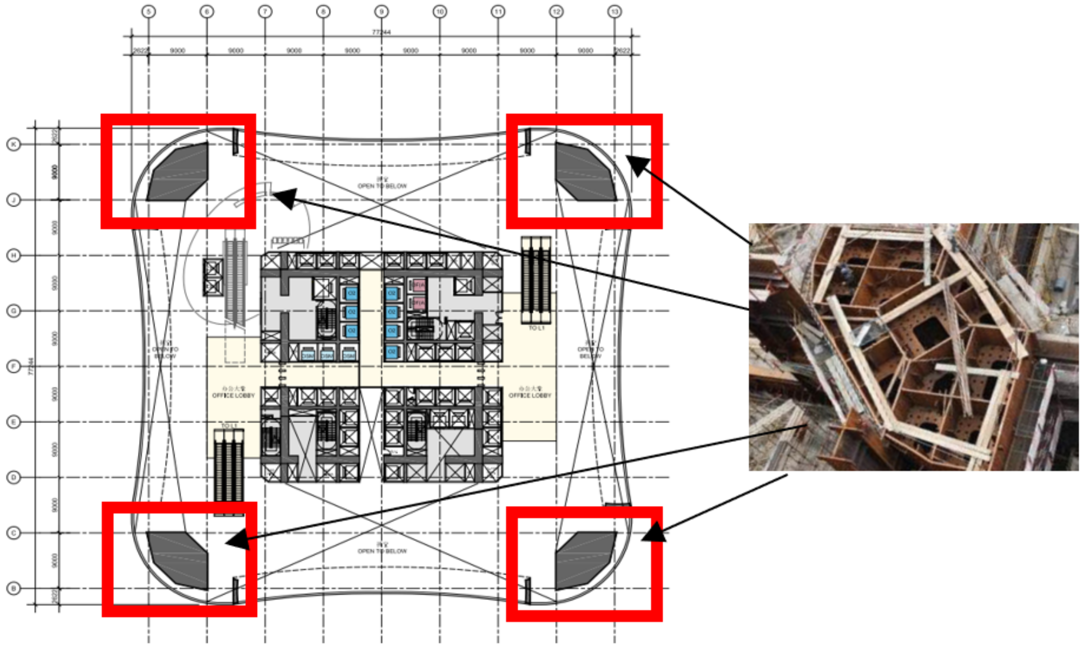

Fig. 1. Application of the irregular hexagoanl section mega columns in high-rise building (Xu et al. [30]).

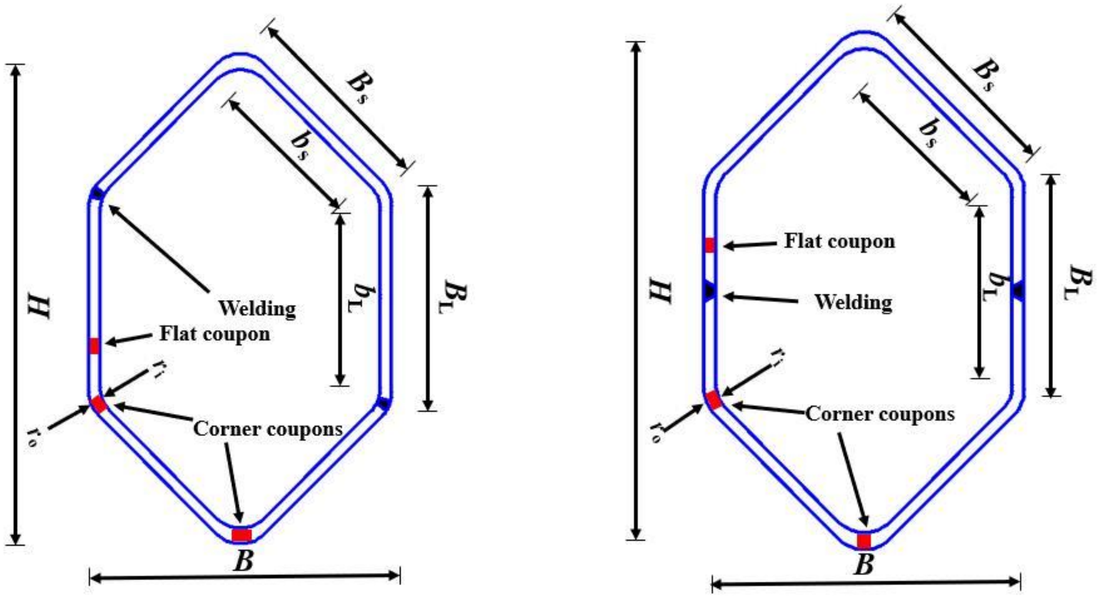

(a) CF1 series

(b) CF2 series

Fig. 2. Two different fabrication methods for cold-formed HSS irregular hexaognal sections.

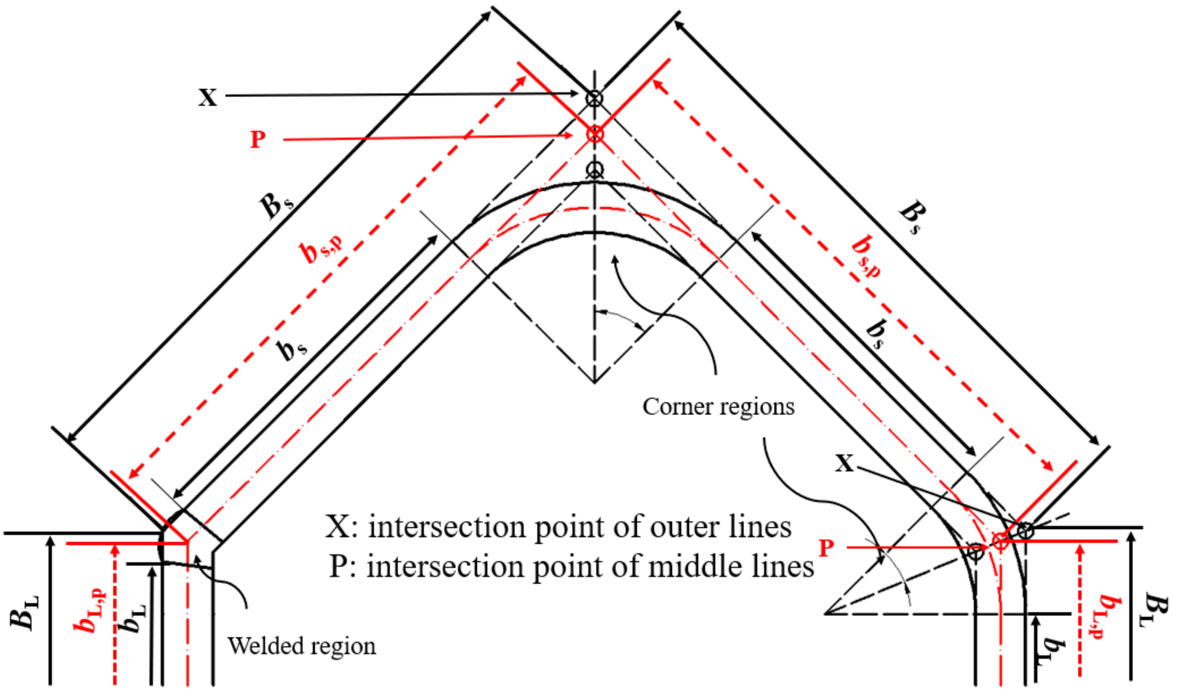

(a) CF1 series of the cold-formed sections

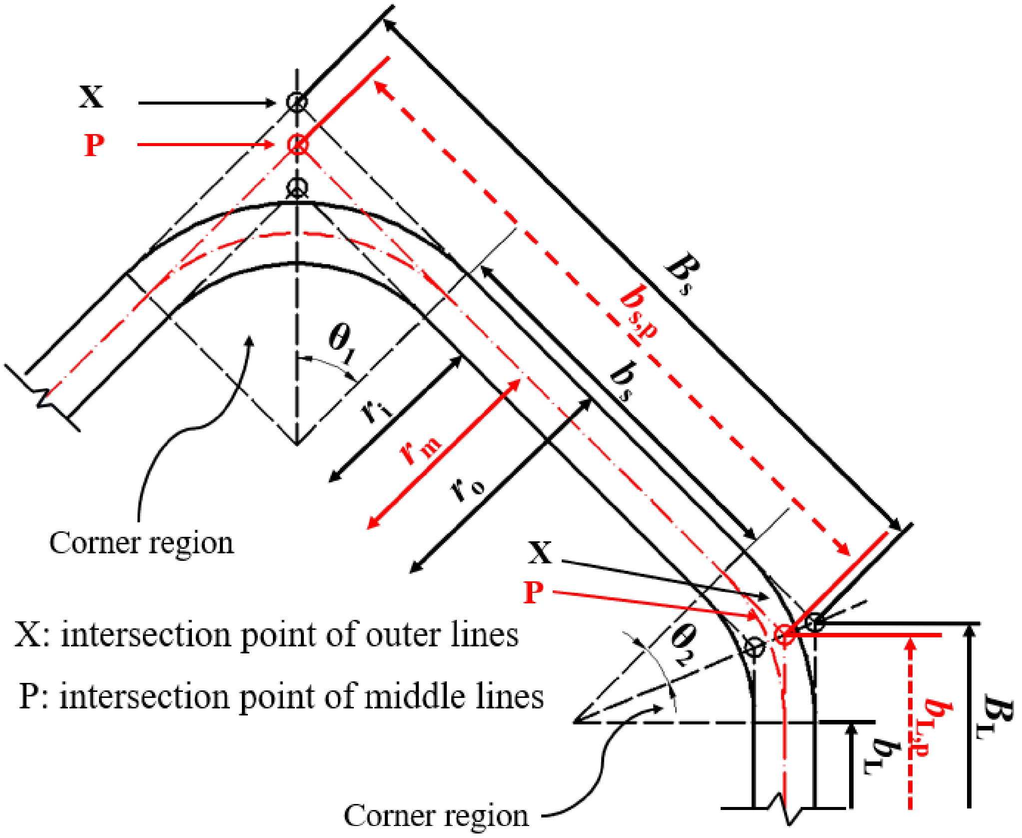

(b) CF2 series of the cold-formed sections

Fig. 3. Detailed geometry and defination of symbols.

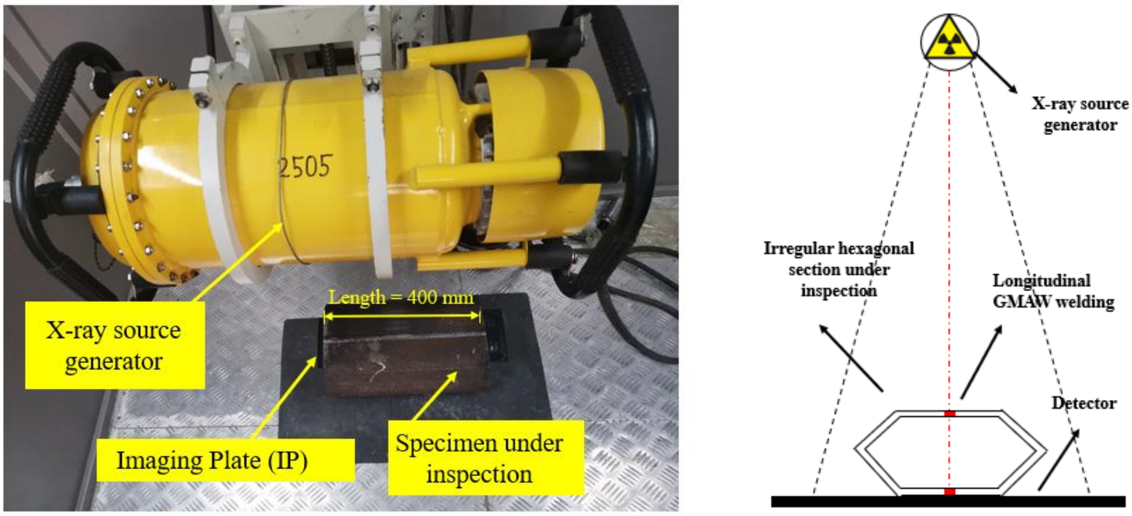

Fig. 4. Schematic view of the X-ray inspection for welding.

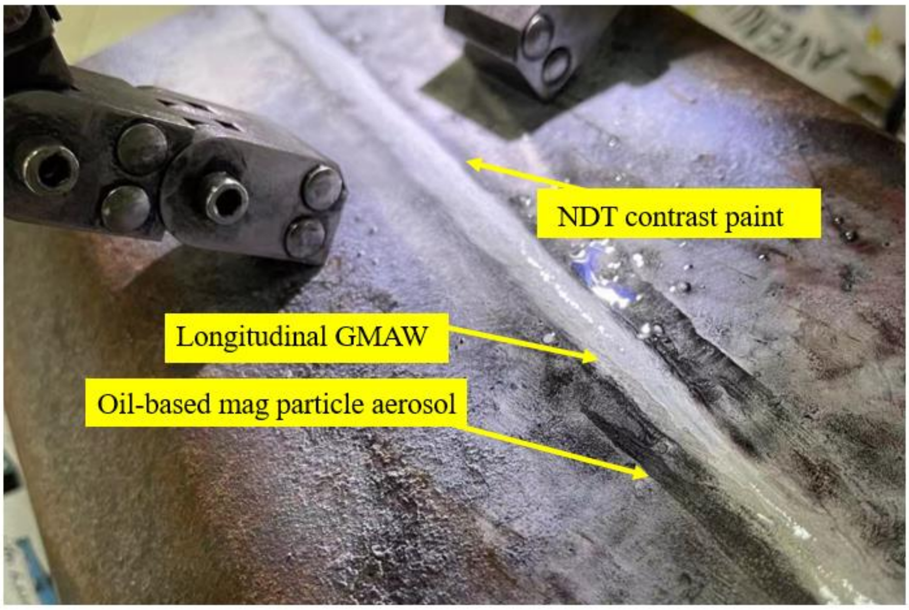

(a) Magenetic particle inspection of surface crack detection for weldment

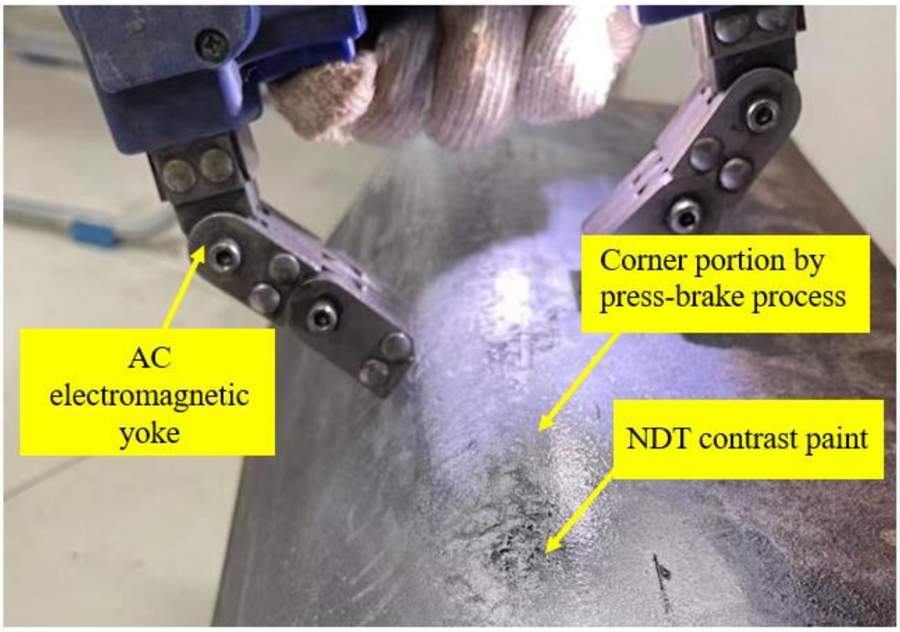

(b) Magenetic particle inspection of surface crack detection for corner portion

Fig. 5. Magnetic particle inspection for surface crack detection.

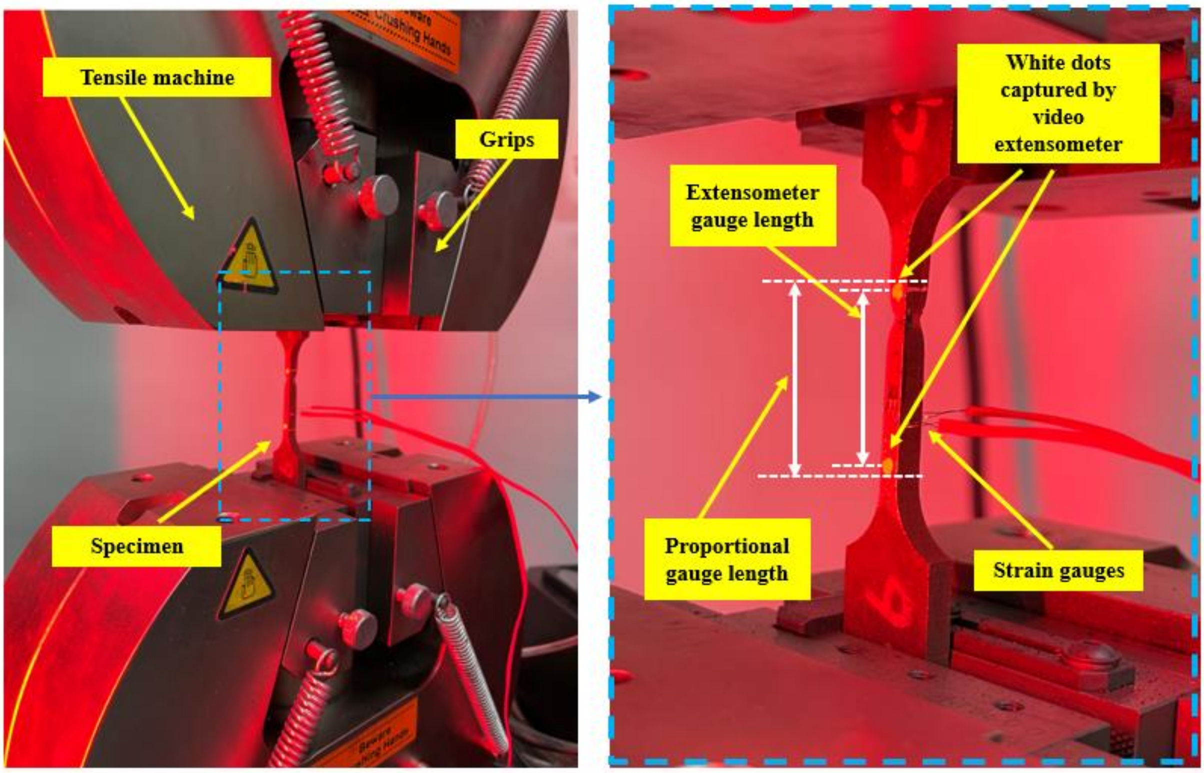

Fig. 6. Test arrangement for the flat and parent coupons.

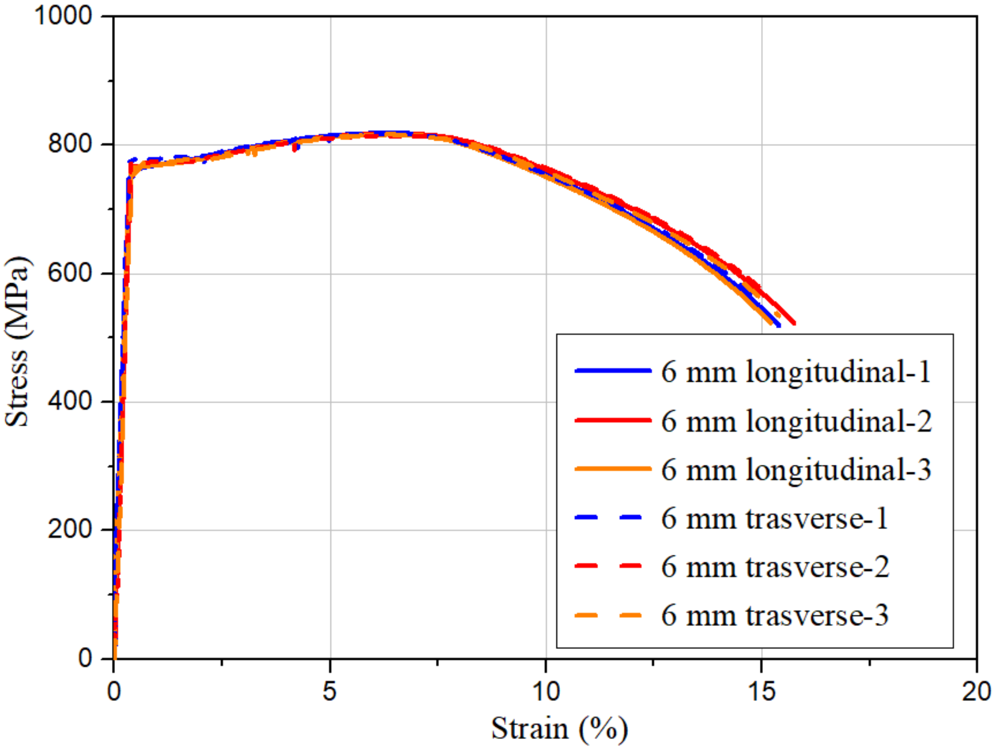

(a)

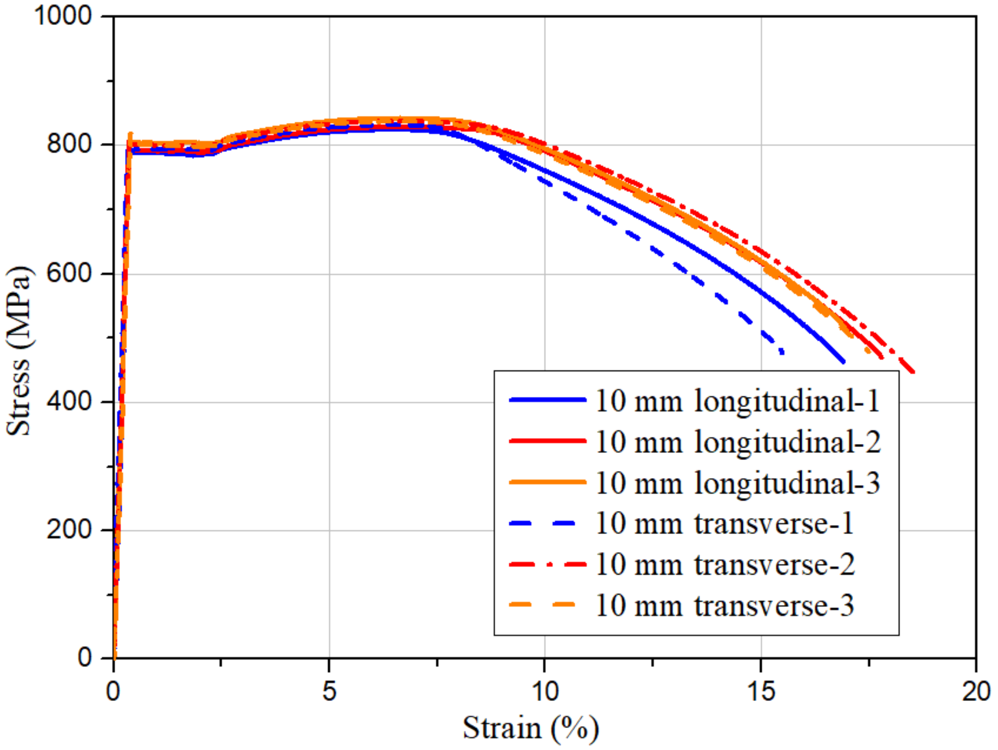

(b)

Fig. 7. Stress-strain curves of the tensile coupon specimens taken from parent plates with thickness of (a) 6 mm and (b) 10 mm.

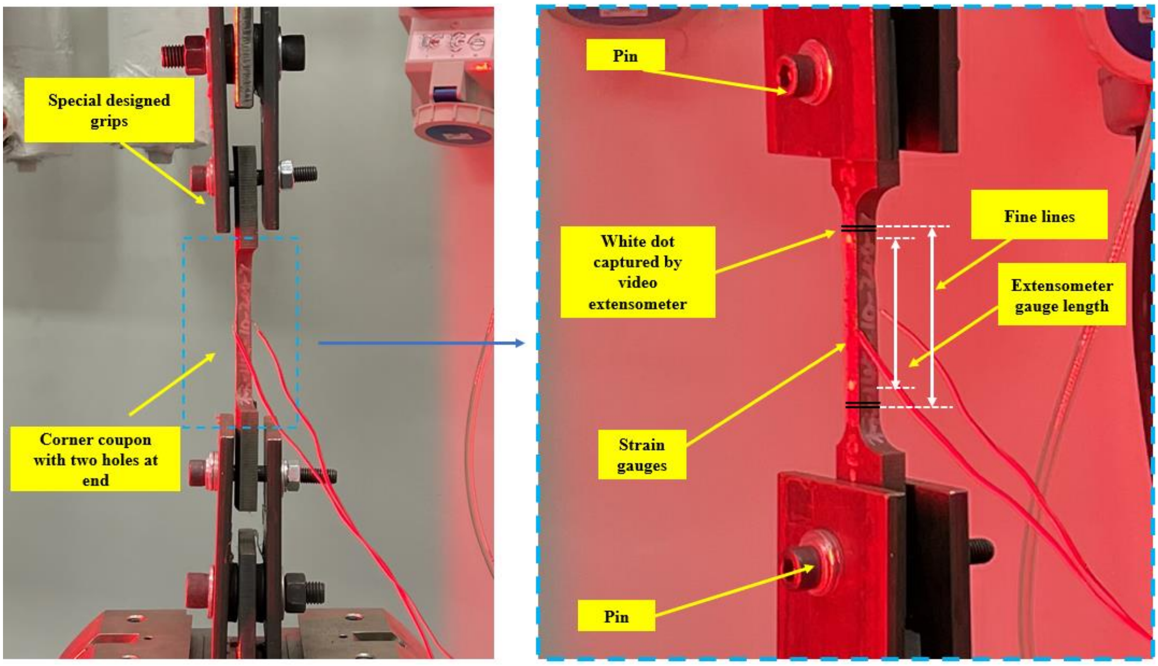

Fig. 8. Test arragement for the corner and welding coupons.

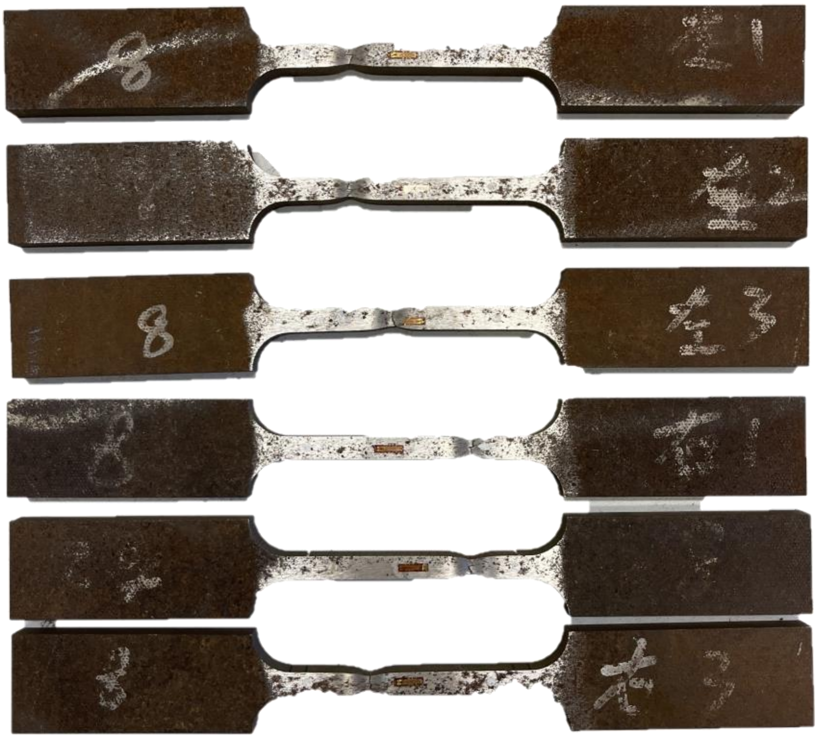

(a)

(b)

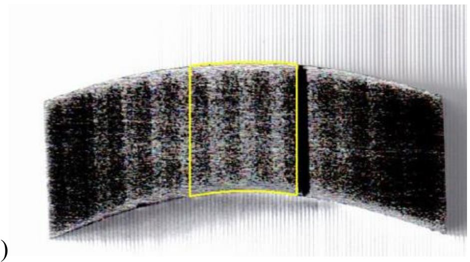

(c)

Fig. 9. Fractued coupons and the CAD scanned cross section. (a) Fractured coupon from 10 mm parent plate (b) Fractured coupons within the cross section of CF2-220 × 6-2.00 (c) CAD scanned cross section of the corner coupon.

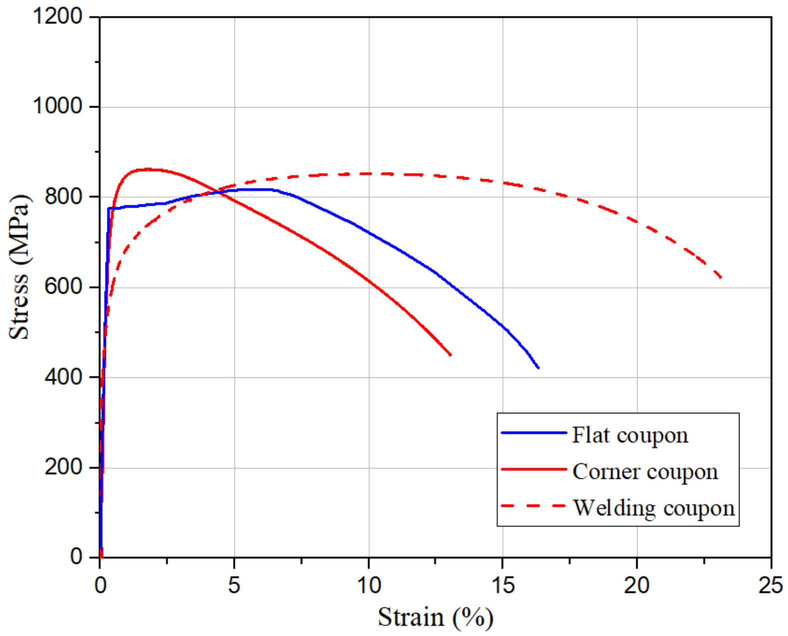

Fig. 10. Comparisons between the stress-strain curves among flat coupon, corner coupon and welding coupon for CF2-220 × 6-2.00.

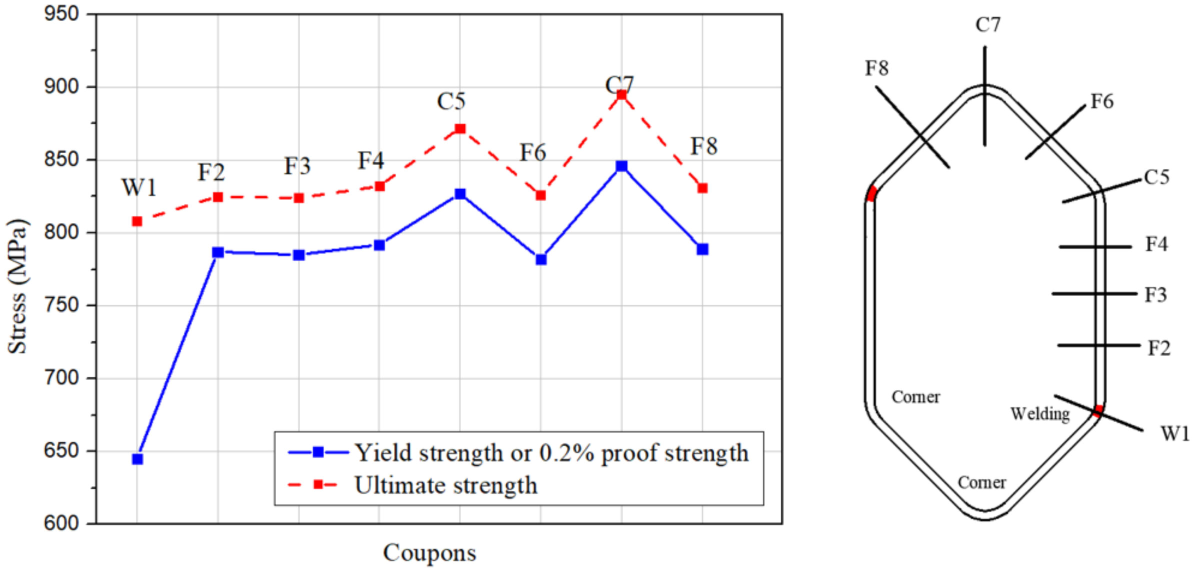

Fig. 11. Distribution of the yield strength or 0.2% proof strength and the ultimate strength within the section of CF1-145 × 6-1.75.

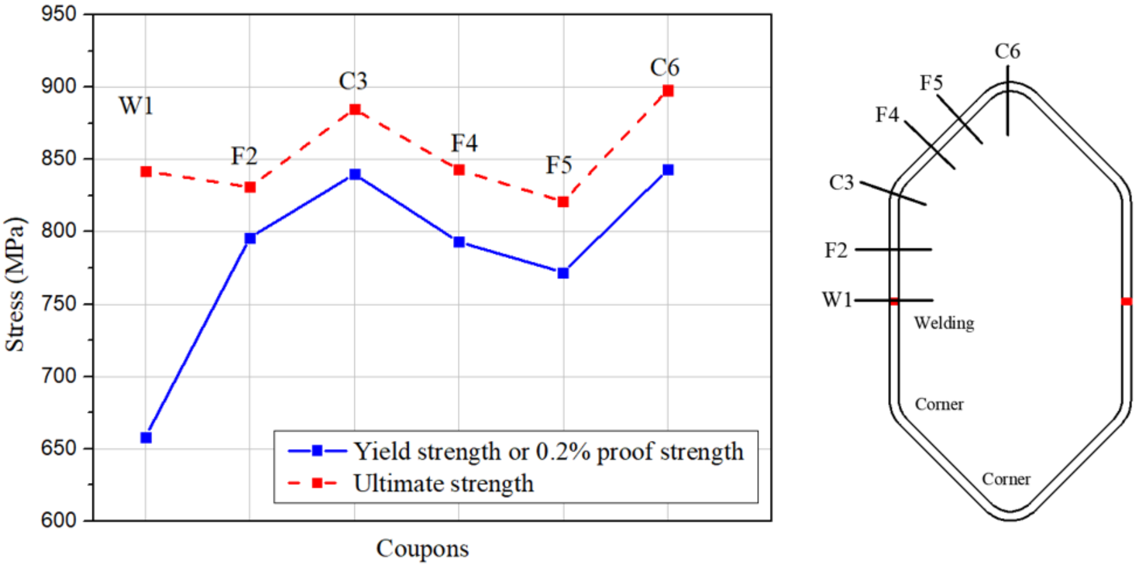

Fig. 12. Distribution of the yield strength or 0.2% proof strength and the ultimate strength within the section of CF2-145 × 6-1.75.

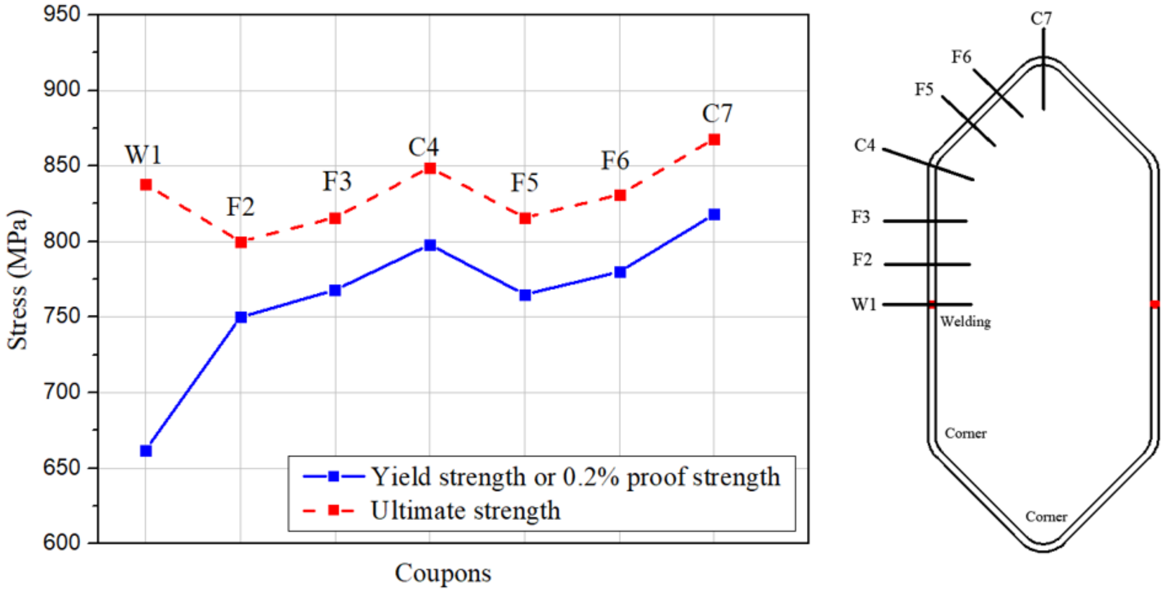

Fig. 13. Distribution of the yield strength or 0.2% proof strength and the ultimate strength within the section of CF2-220 × 6-2.00.

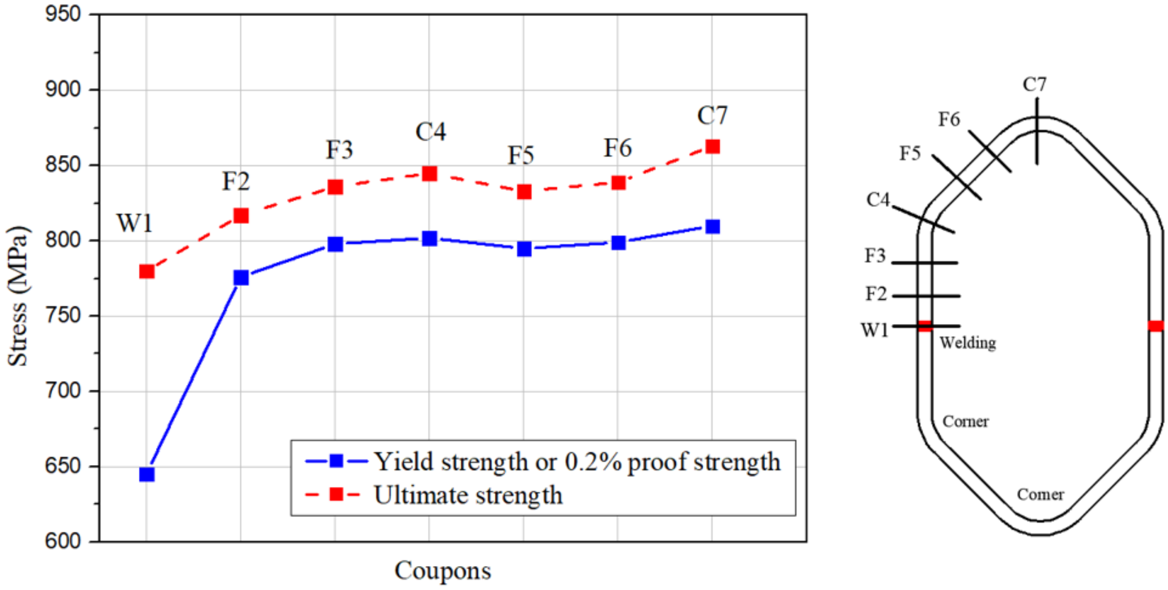

Fig. 14. Distribution of the yield strength or 0.2% proof strength and the ultimate strength within the section of CF2-145 × 10 -1.75.

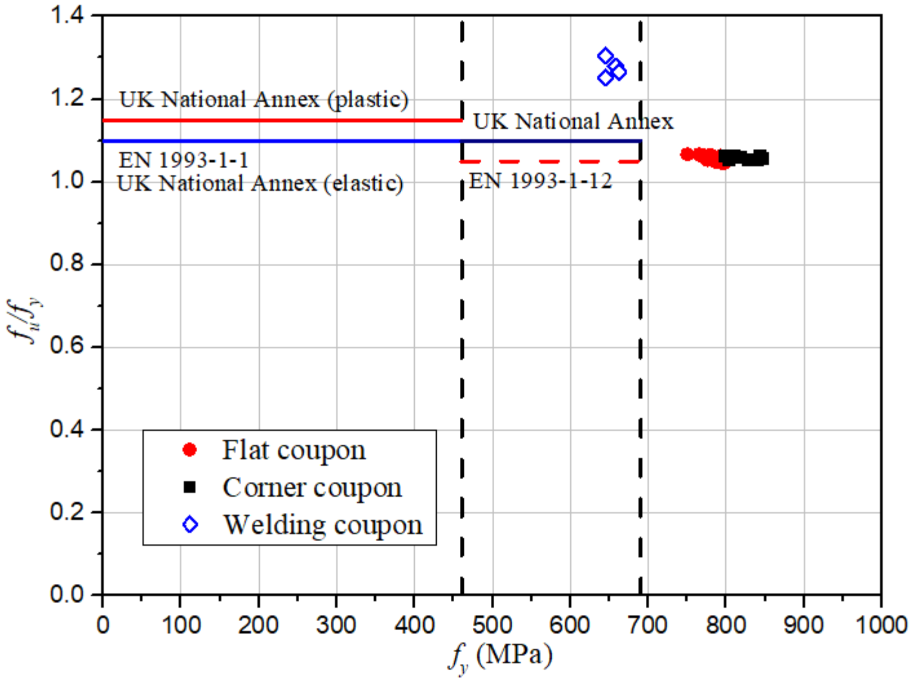

Fig. 15. Requirements on the ratio between ultimate strength and yield strength.

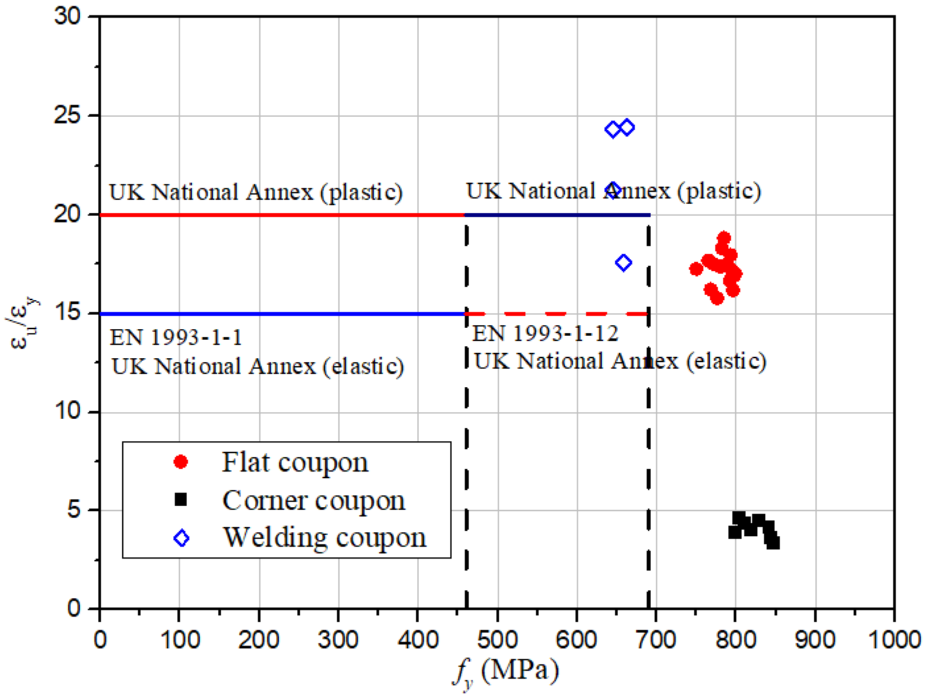

Fig. 16. Requirements on the ratio between ultimate strain and yield strain.

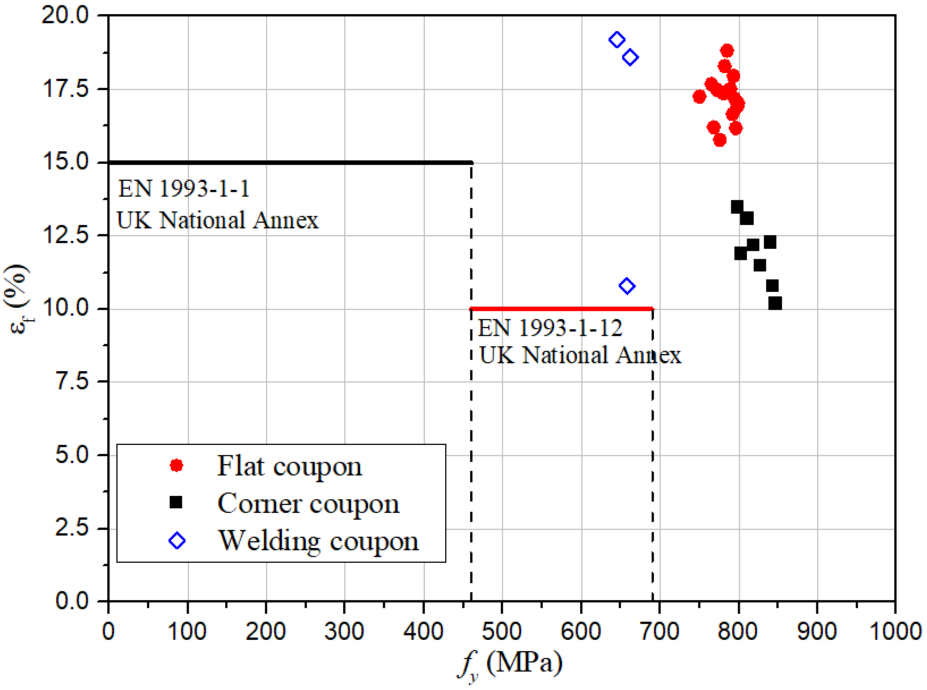

Fig. 17. Requirements on the elongation at failure.

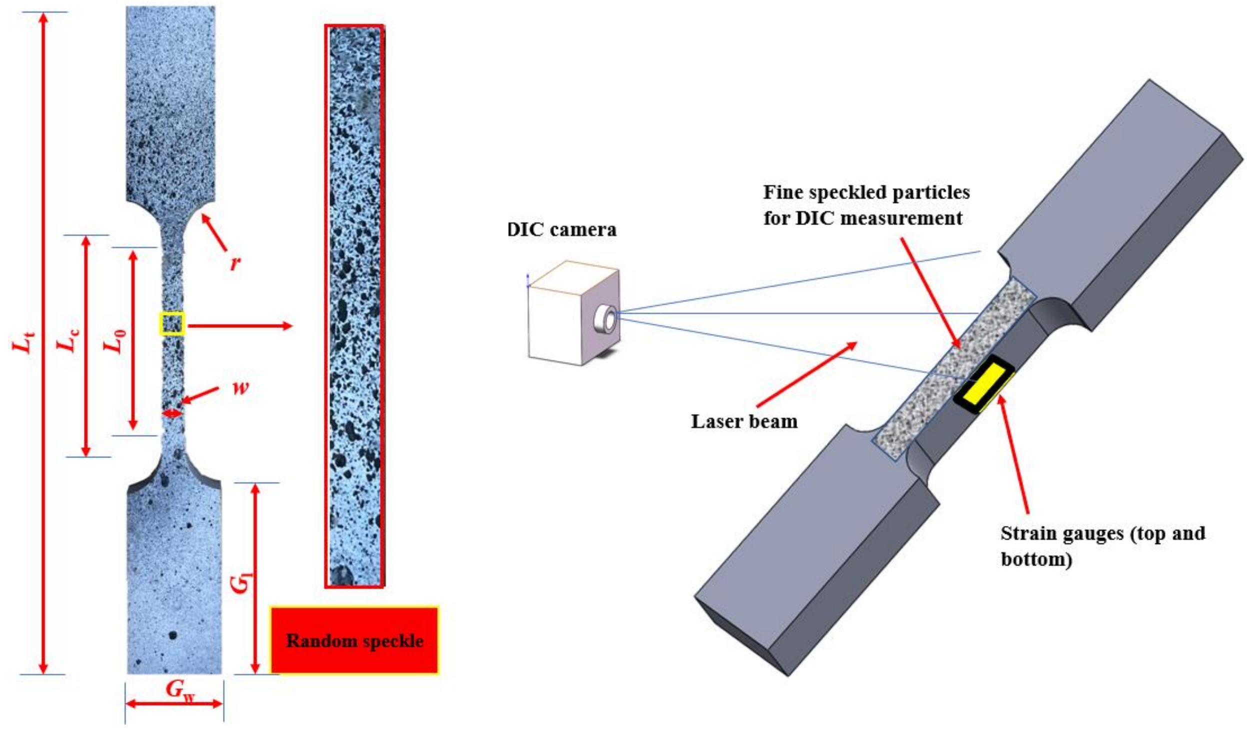

Fig. 18. Preparation of the tensile coupon for DIC method and the mechanism of the DIC measurement.

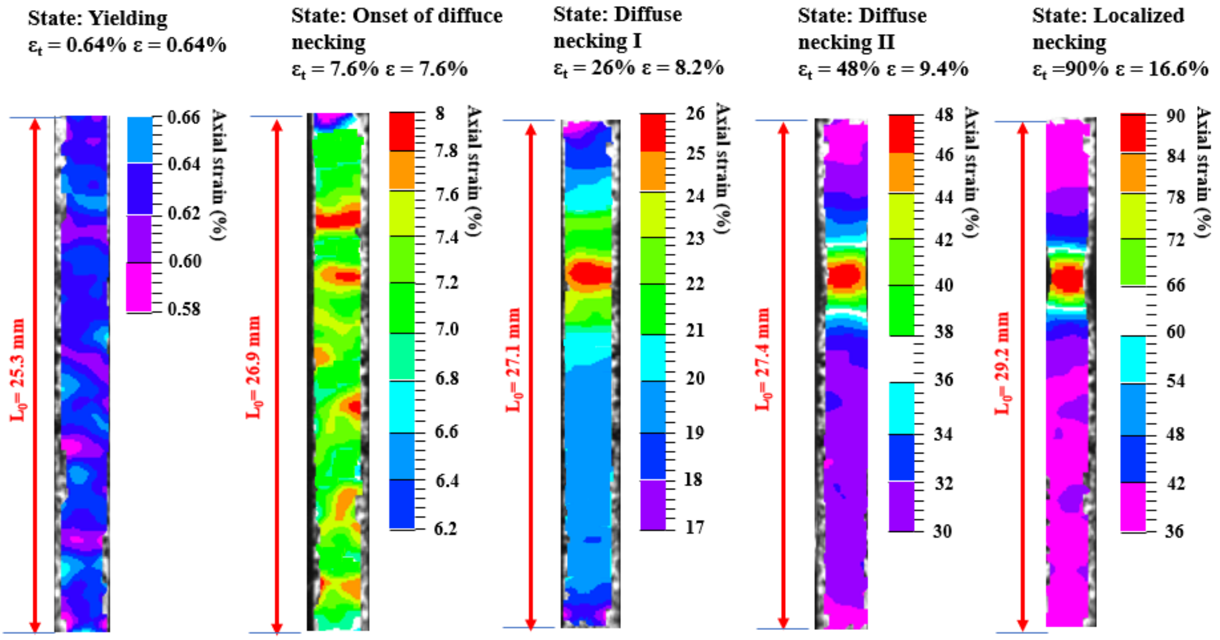

Fig. 19. Obtained test results from DIC measurement for the variations of the strain fields for the full life-cycle deformations for CF2-145 × 6-1.75 – F2D.

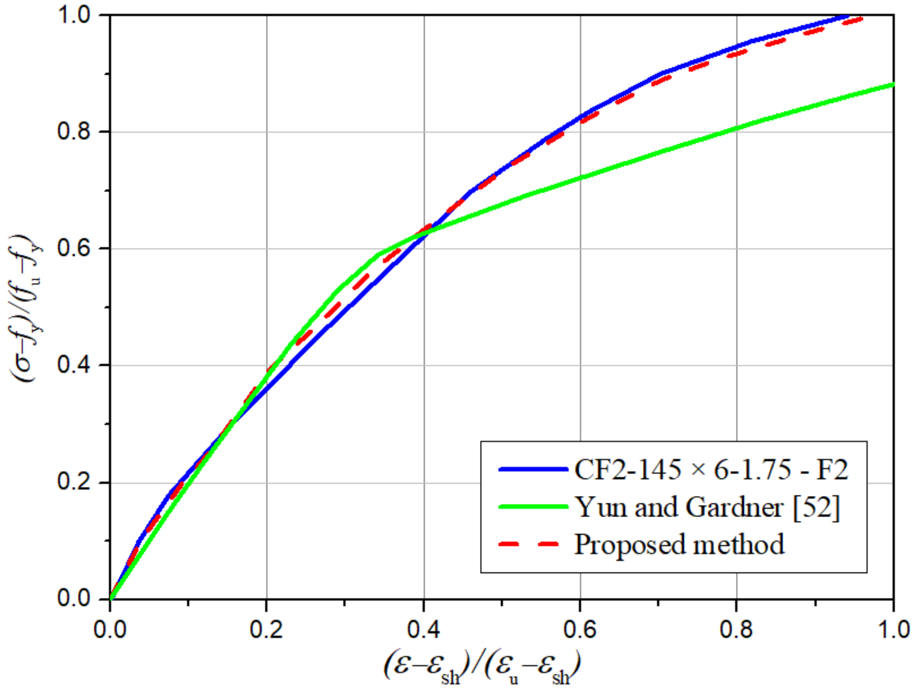

(a) Flat coupon from section of of CF2-145 × 6 -1.75-F2

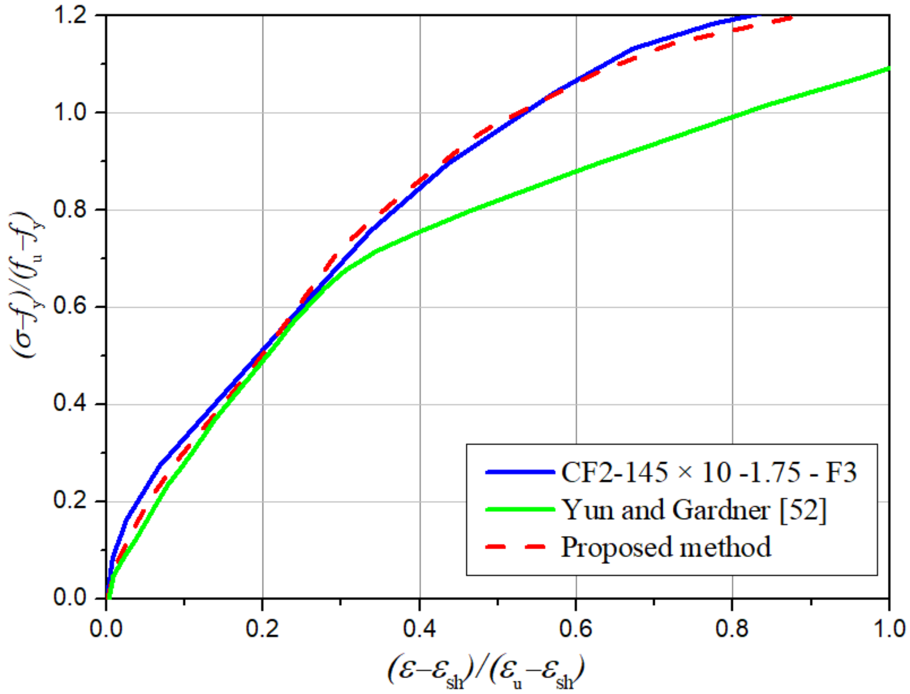

(b) Flat coupon from section of of CF2-145 × 10-1.75-F3

Fig. 20. Comparison of the proposed model with test results with yield plateau.

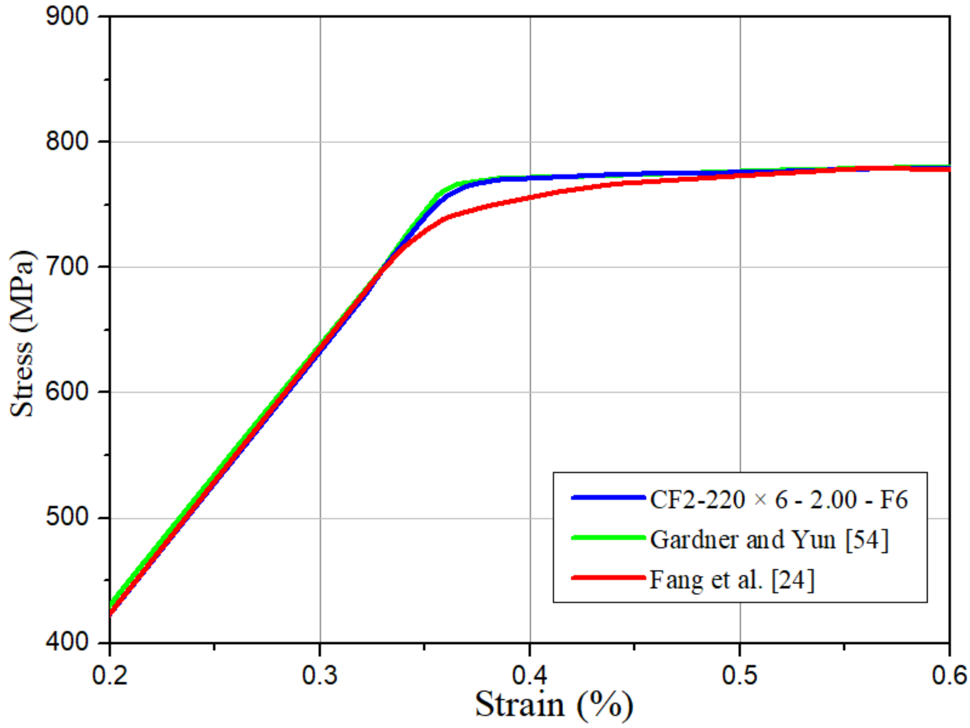
900
800
700
600
500
400
Stress (MPa)
0.2
0.3
0.4
0.5
0.6
Strain (%)
CF2-220 × 6 - 2.00 - F6
Gardner and Yun [54]
Fang et al. [24]

(a)

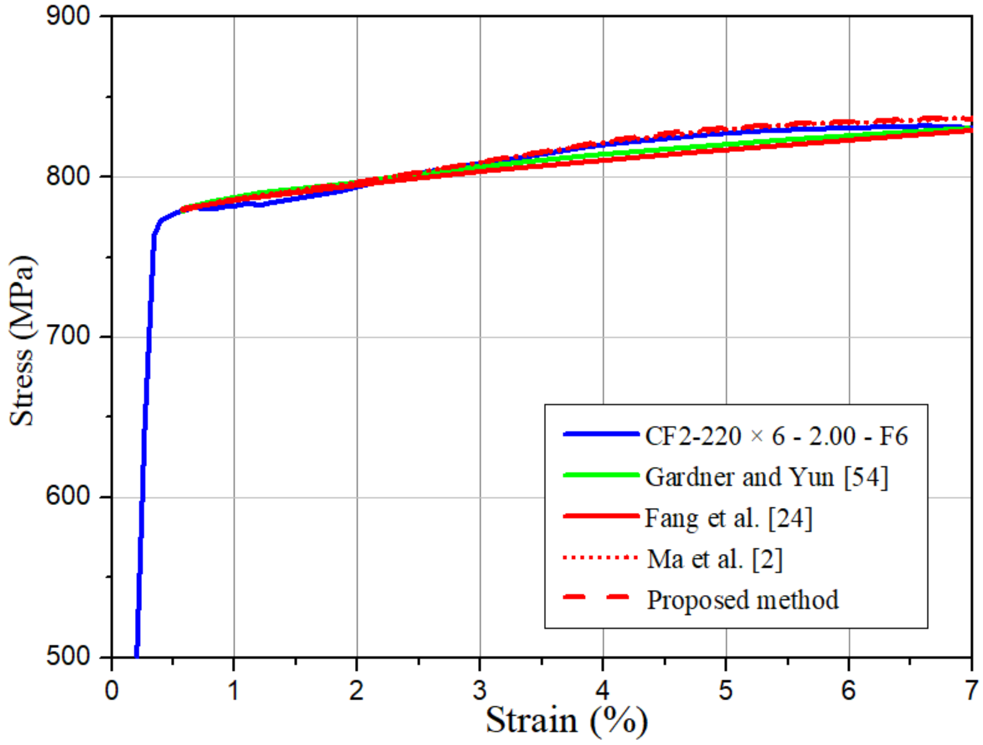
900
800
700
600
500
Stress (MPa)
0
1
2
3
4
5
6
7
Strain (%)
CF2-220 × 6 - 2.00 - F6
Gardner and Yun [54]
Fang et al. [24]
Ma et al. [2]
Proposed method

(b)

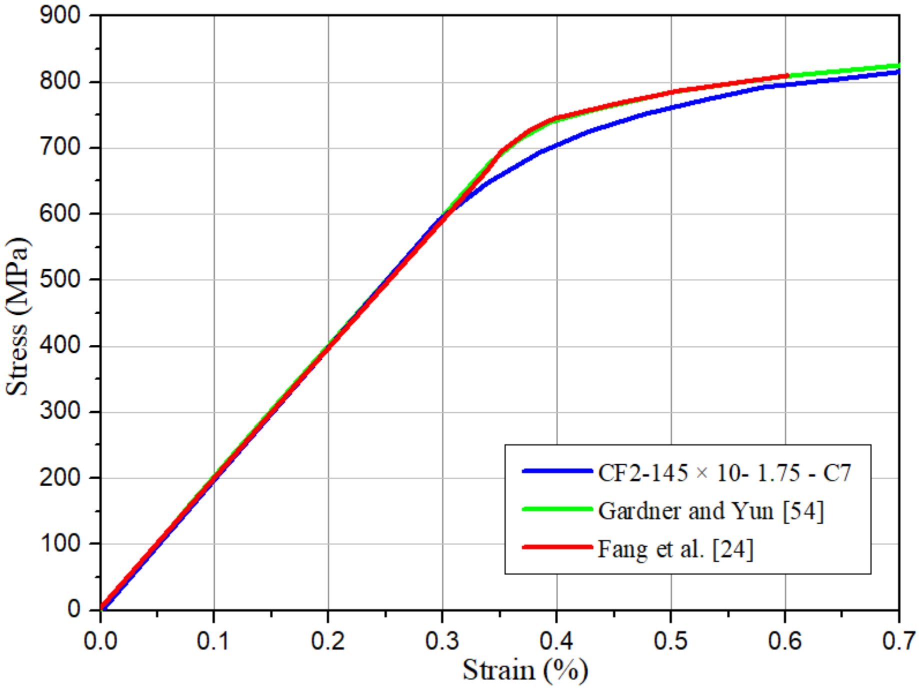

(c)

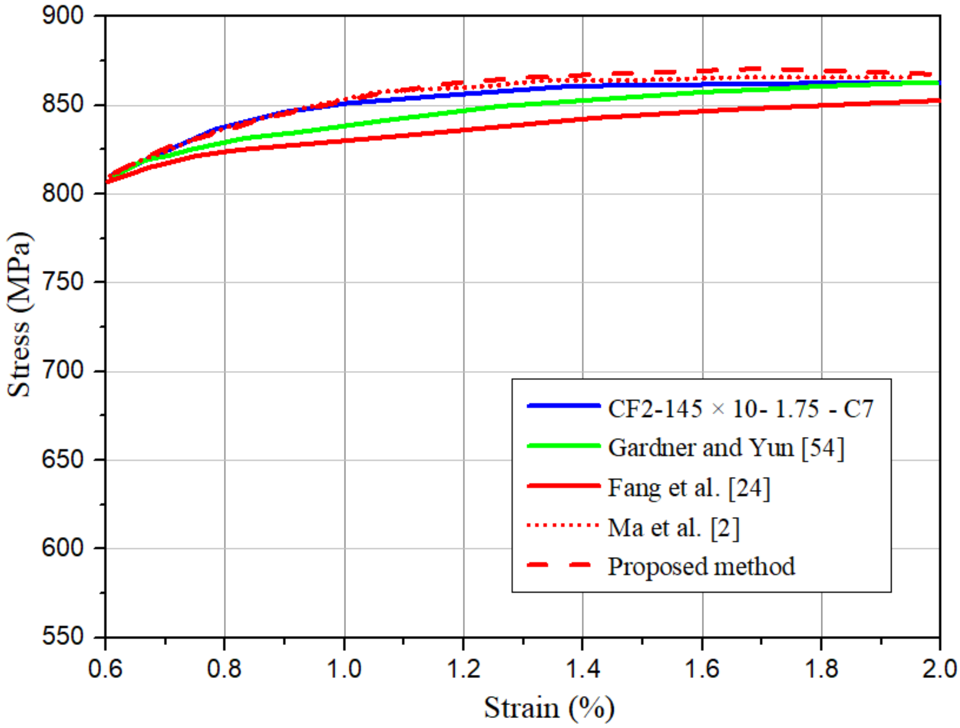

(d)

Fig. 21. Comparison of the predict models with the experimental results of the flat and corner coupons taken from the sections (a) Flat coupon from section of of CF2-220 × 6-2.00-F6 in intial stage (b) Flat coupon from section of of CF2-220 × 6-2.00-F6 in second hardening stage (c) Corner coupons from the section of CF2-145 × 10-1.75-C7 in initial stage (d) Corner coupons from the section of CF2-145 × 10-1.75-C7 in second stage.

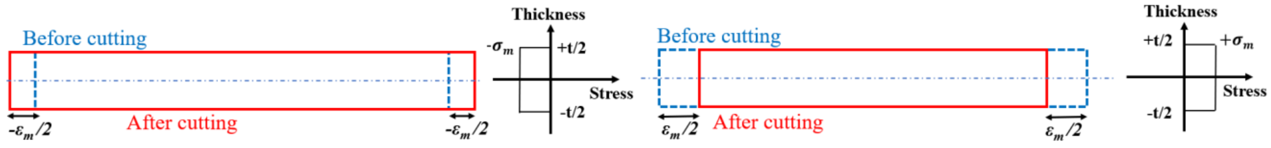

(a) Membrane residual stress

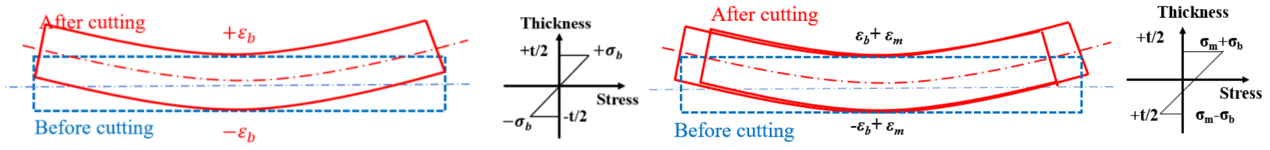

(b) Bending residual stress (c) Combined bending and tensile membrane residual stresses

Fig. 22. Effects of membrane and bending residual stresses.

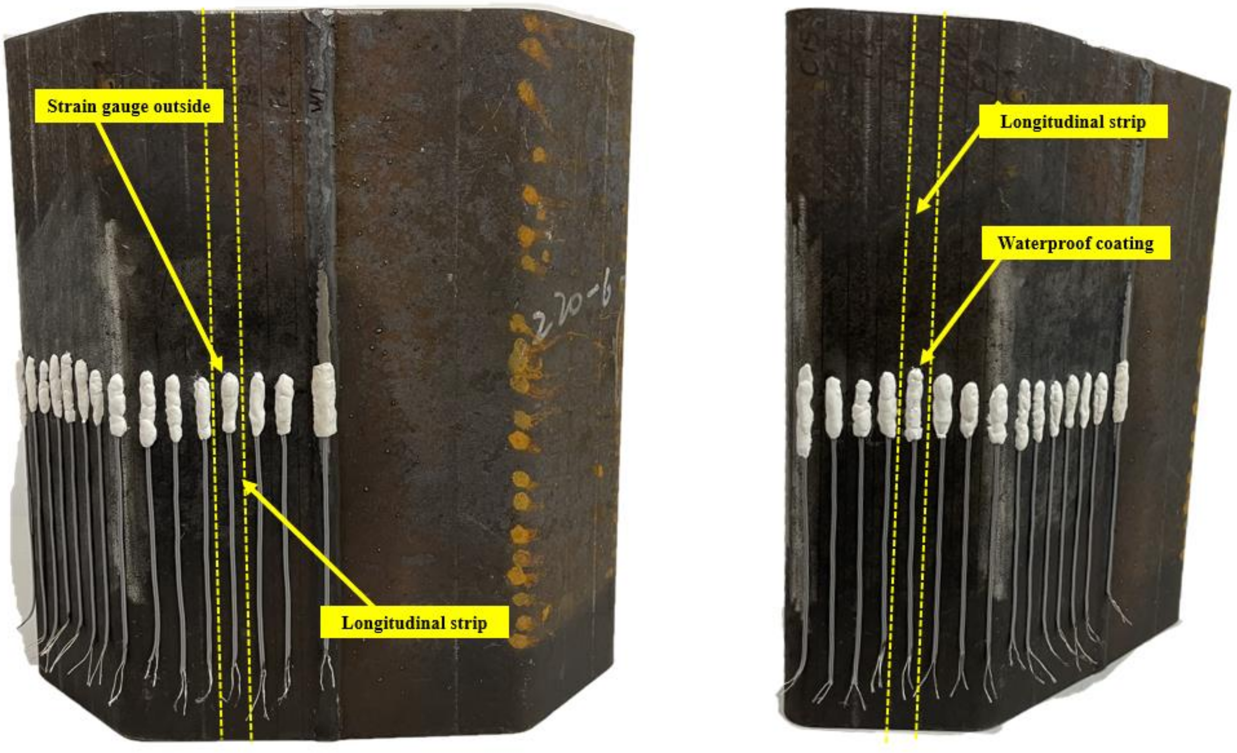

(a) Test arrangement of the outer strain gauges

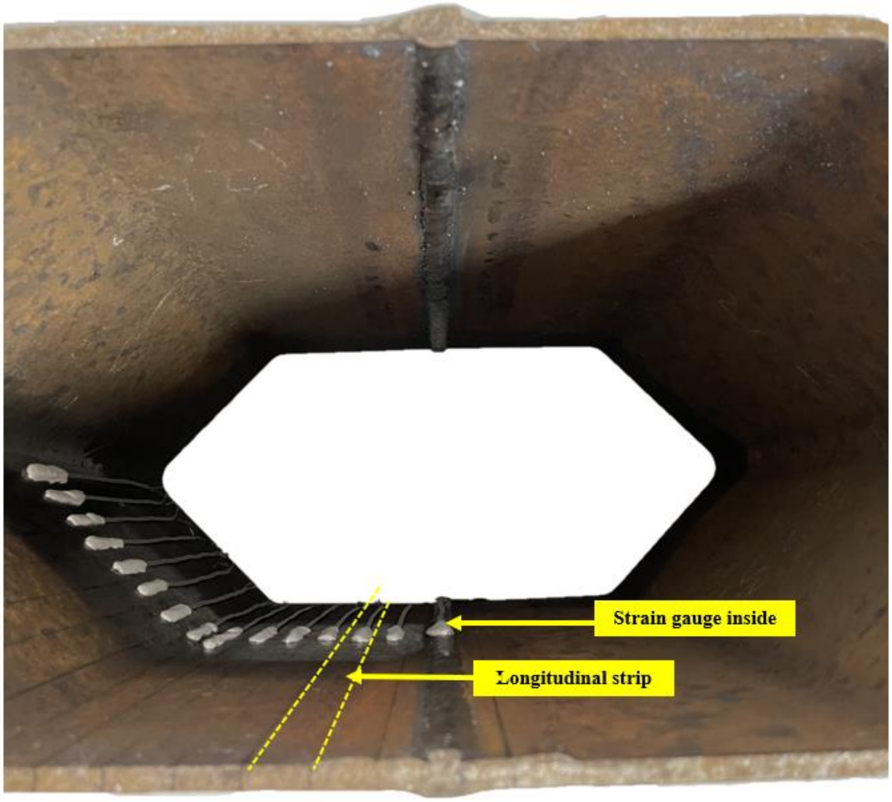

Fig. 23. Prepared specimen CF2-220 × 6-2.00 with outer and inner electric strain gauge ready for sectioning process.

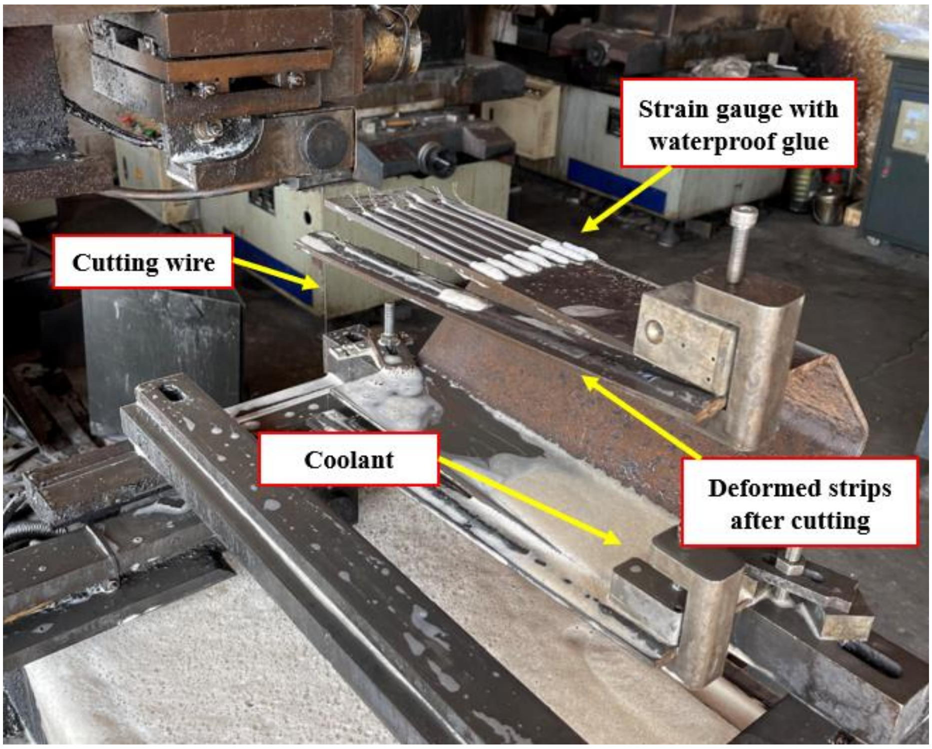

Fig. 24. Sectioning process using wire-cutting with coolant.

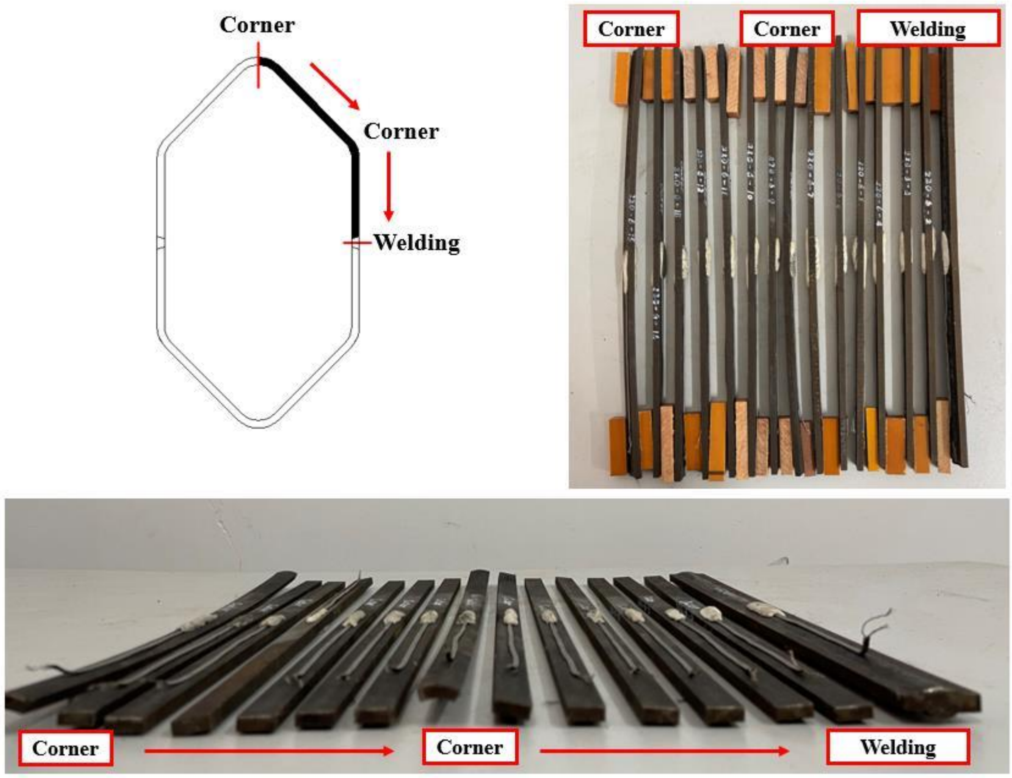

Fig. 25. Deformed strips extracted from CF2-220 × 6 – 2.00 after sectioning process.

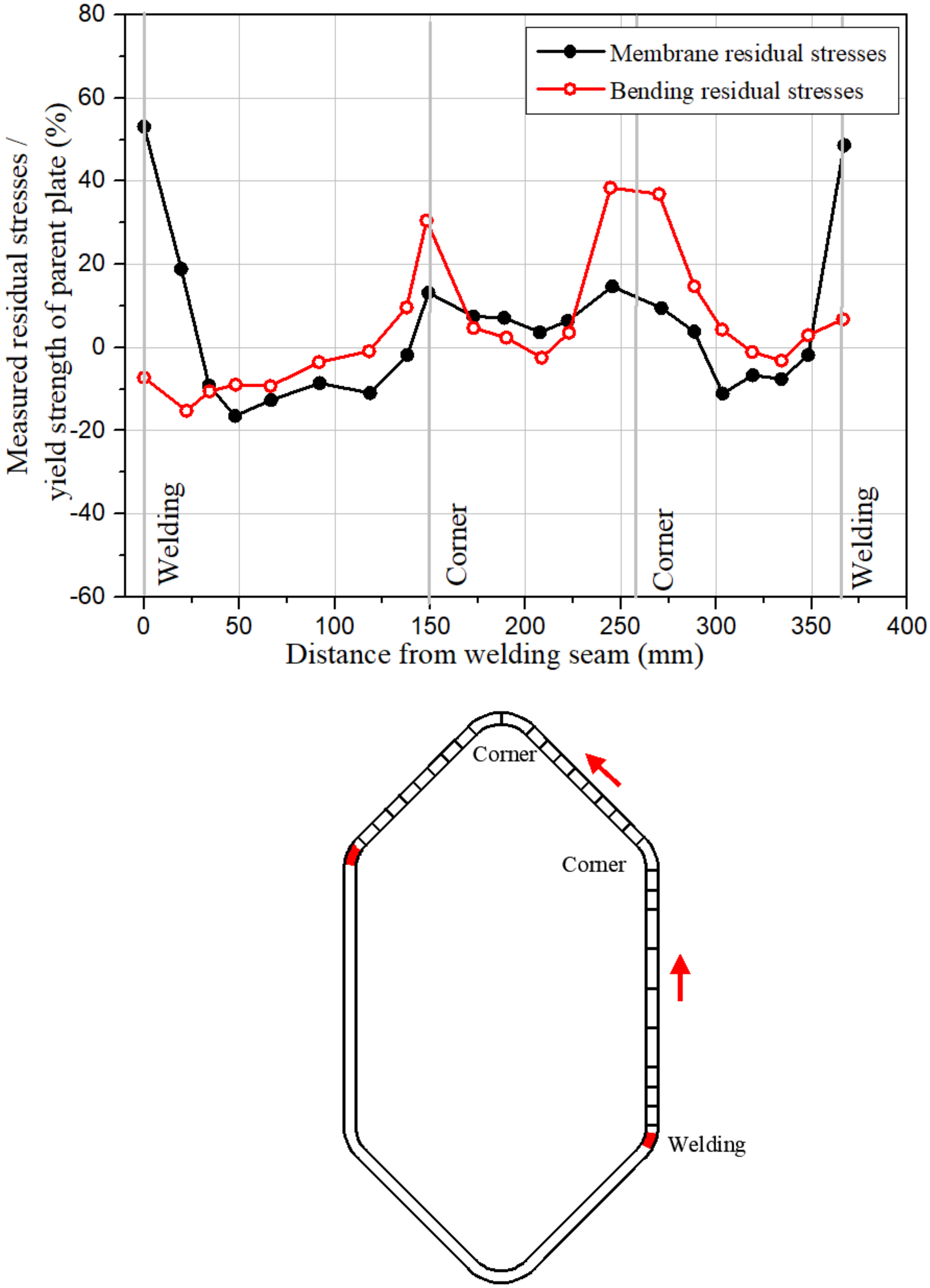

Fig. 26. Magnitude and the distribution of the longitudinal residual stresses in CF1-145 × 6-1.75.

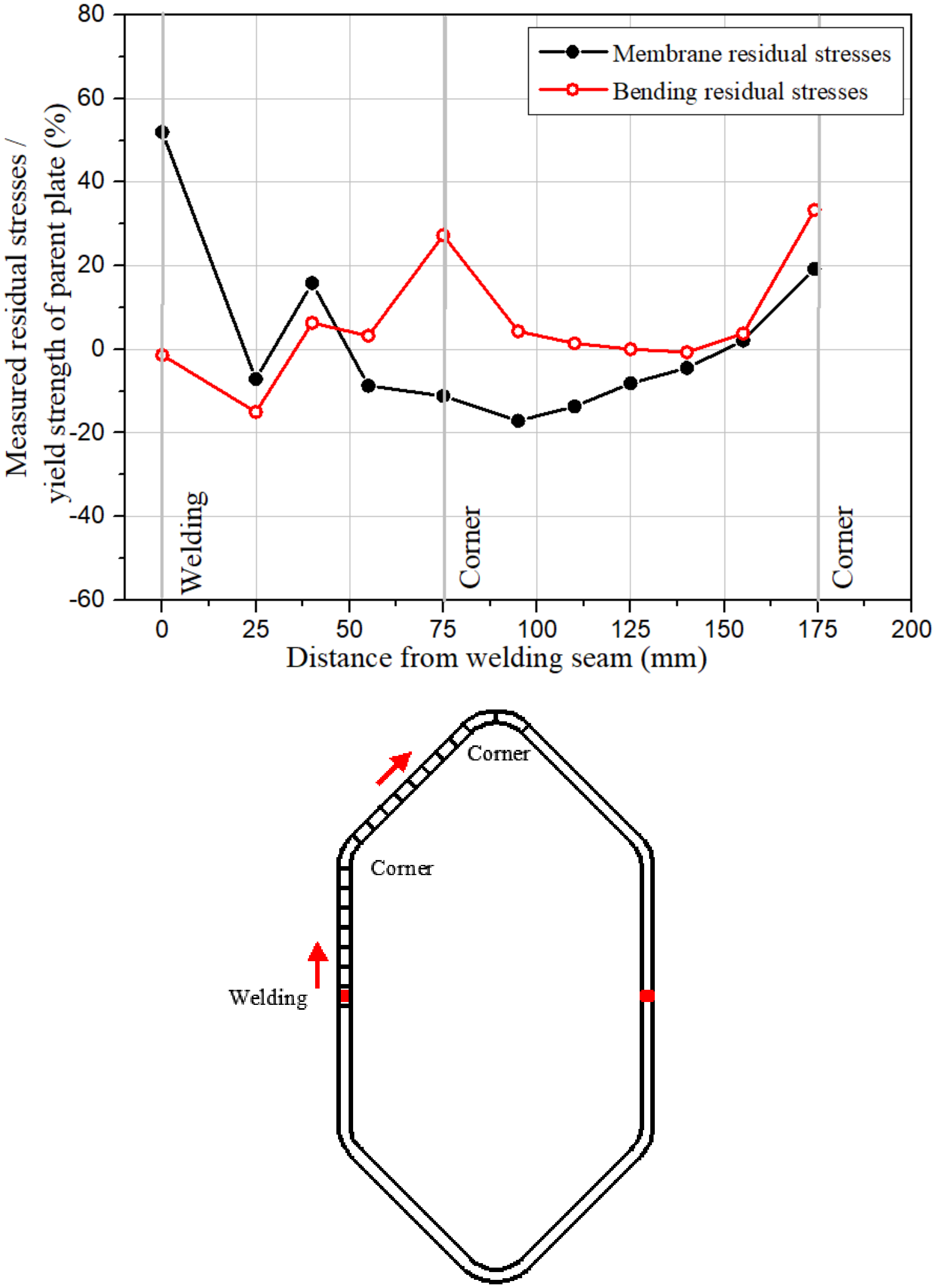

Fig. 27. Magnitude and the distribution of the longitudinal residual stresses in CF2-145 × 6-1.75.

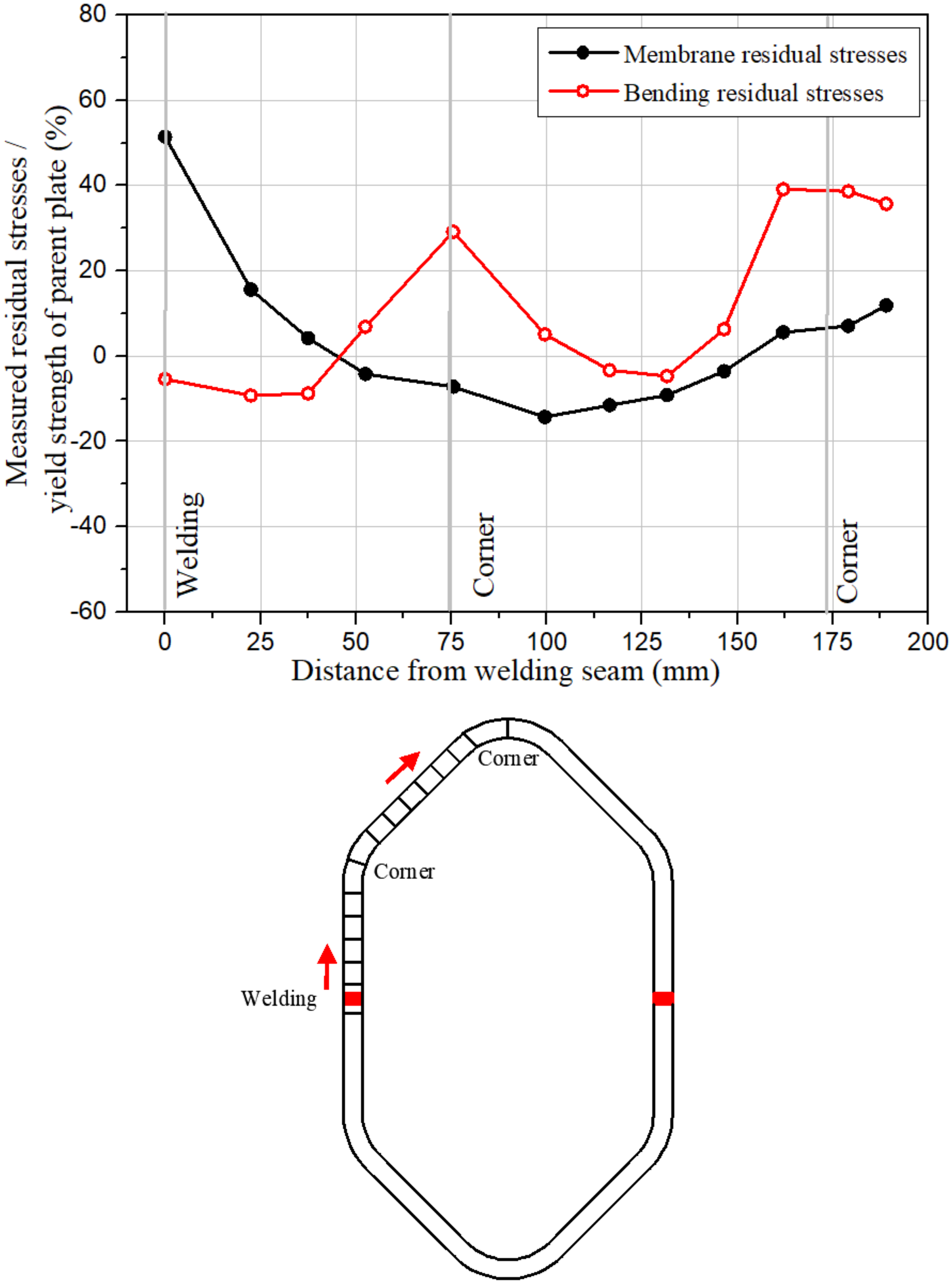

Fig. 28. Magnitude and the distribution of the longitudinal residual stresses in CF2--145 × 10-1.75.

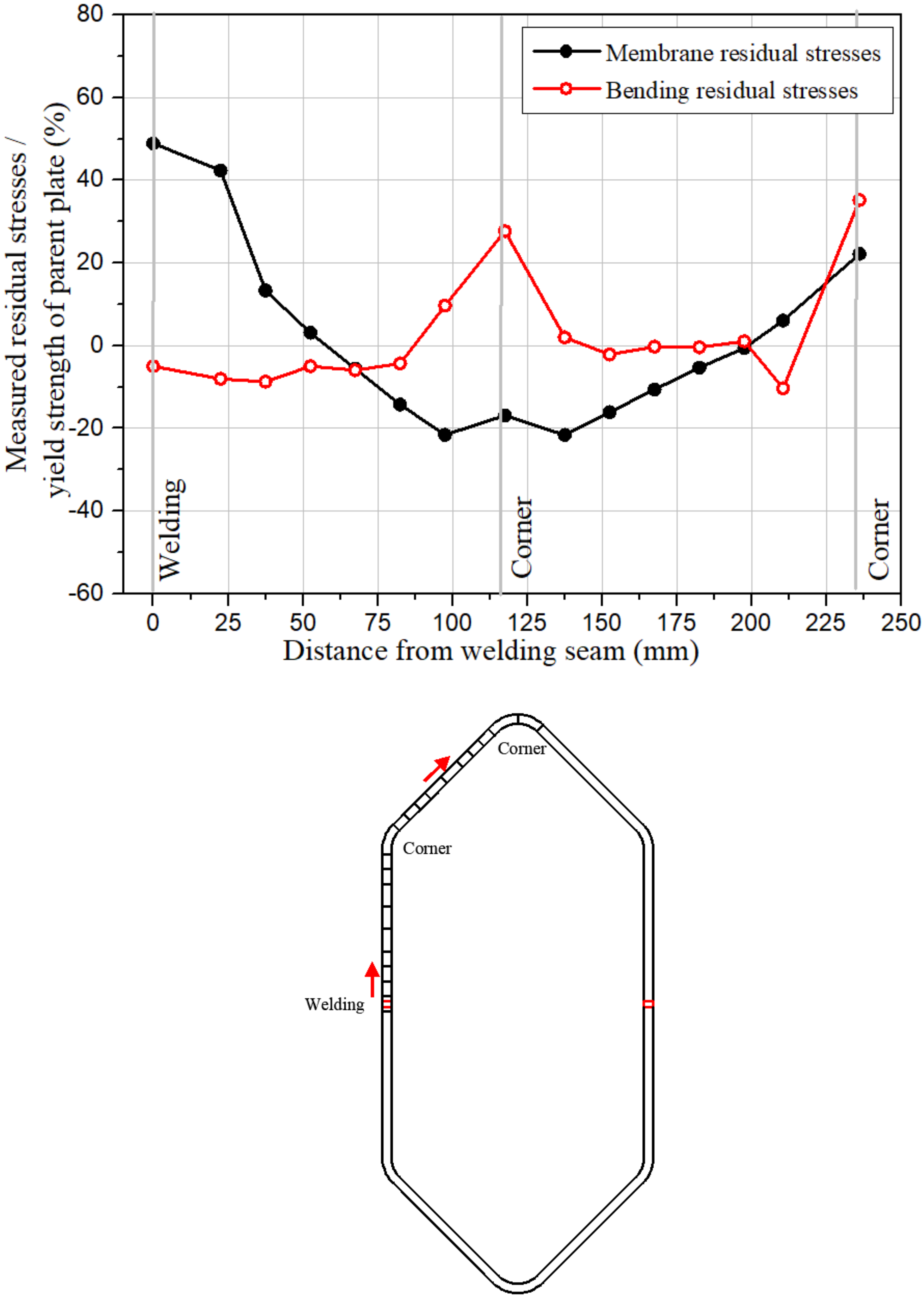

Fig. 29. Magnitude and the distribution of the longitudinal residual stresses in CF2-220 × 6-2.00.

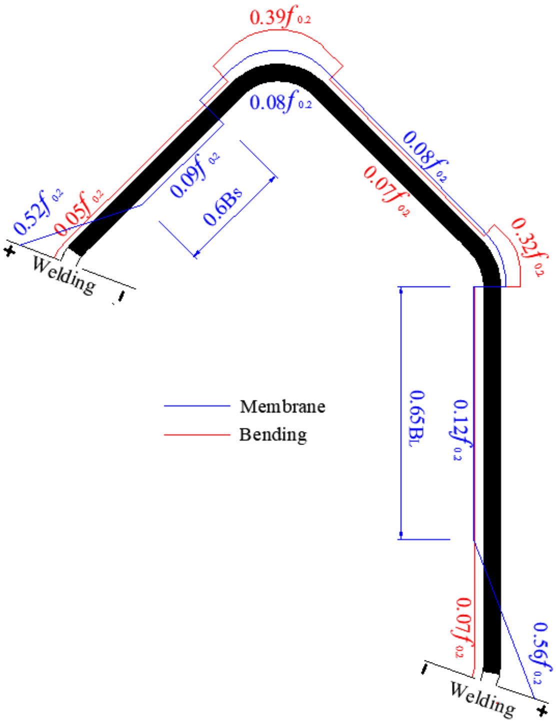

Fig. 30. Residual stress predictive model for CF1-series irregular hexagonal hollow sections.

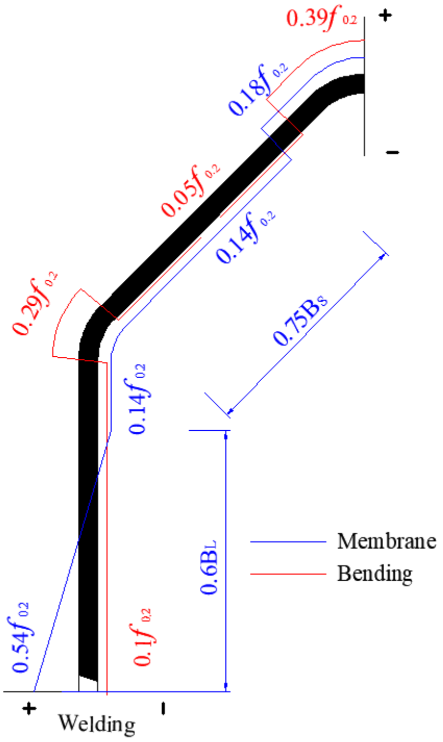

Fig. 31. Residual stress predictive model for CF2-series irregular hexagonal hollow sections.

Table 1 Chemical composition listed in mill certificates.

Steel plate	Chemical composition (wt%)										
	C	Mn	P	S	Si	Cr	Mo	Nb	Ti	B	CEV
6 mm plate	0.13	1.39	0.011	0.001	0.26	0.27	0.14	0.027	0.015	0.002	0.45
10 mm plate	0.14	1.41	0.012	0.001	0.26	0.26	0.15	0.025	0.014	0.002	0.46
EN 10025-6 [48][a]	0.22	1.80	0.025	0.012	0.86	1.60	0.74	0.07	0.07	0.006	–

[a]Indicates that upper limit

Table 2 Chemical composition of the welding electrode ER100S-G and ER110S-G.

Electrode	Chemical composition (wt%)										
	C	Mn	P	S	Si	Cr	Mo	Nb	Ti	V	Ni
ER100S-G	0.08	1.70	0.008	0.008	0.60	0.20	0.50	0.027	0.05	0.005	1.50
ER110S-G	0.09	1.70	0.009	0.008	0.70	0.30	0.60	0.027	0.1	0.03	1.85

Table 3 Linear heat input for the welding passes.

Specimens	Welding Pass number	Current I (A)	Voltage U (V)	Welding speed v (mm/s)	Linear heat input energy q (kJ/mm)[a]
CF1-145×6-1.75	1[b]	130	19.5	3.5	0.62
	2[c]	192	22.6	4.2	1.05
CF2-145×6-1.75	1[b]	142	20.1	3.2	0.69
	2[c]	192	21.8	4.5	1.02
CF2-220×6-2.00	1[b]	125	19.5	3.0	0.59
	2[c]	190	23.6	4.2	1.09
CF2-145×10-1.75	1[b]	135	20.4	3.4	0.67
	2[c]	190	23.8	4.5	1.10

[a] The linear heat input energy is derived as $q = k \times U \times I/(v \times 1000)$ where k is the thermal coefficient taken as0.8 for GMAW [31]; [b] refers to the backing welding; [c] indicates the second welding pass.

Table 4 Measured dimensions of cold-formed HSS irregular hexagonal hollow section specimens.

Specimens	Edge length B_s (mm)	Side width b_s (mm)	Edge length B_L (mm)	Side width b_L (mm)	Thickness t (mm)	Inner radius r_i (mm)
CF1-145×6-1.75	110.2	75.8	148.2	136.5	5.83	17.8
CF2-145×6-1.75	110.5	76.5	148.7	128.8	5.81	17.9
CF2-220×6-2.00	123.9	90.0	222.9	203.0	5.76	17.7
CF2-145×10-1.75	121.6	65	153.1	120	9.90	28.8

Table 5 Ductility requirements in different specifications for Q690 steel or its equivalent grade steel.

Countries or regions	Standard	Steel grades (nominal yield strengths in MPa)	Requirements on ductility
Australia	AS 3597-2008 [56]	Grade 700 (690 MPa)	$\varepsilon_{f,50} \geqslant 16\%$
China	GB/T 1591-2008 [57]	Q690 (690 MPa)	$\varepsilon_f \geqslant 14\%$
	GB/T 19879-2015 [58]	Q690GJ (690 MPa)	$f_y/f_u \leqslant 0.85$, $\varepsilon_f \geqslant 14\%$
		70Mn ($\geqslant$ 450 Mpa)	$\varepsilon_f \geqslant 8\%$
	GB/T 699-2015 [59]	75 (880 MPa)	$f_y/f_u \leqslant 0.85$, $\varepsilon_f \geqslant 14\%$
		80 (930 MPa)	$\varepsilon_f \geqslant 8\%$
Europe	EN 1993-1-12 [41]	S500 (500 MPa) to S700 (700 MPa)	$f_u/f_y \geqslant 1.05$, $\varepsilon_f \geqslant 10\%$, $\varepsilon_u \geqslant 15\varepsilon_y$
	EN 10025-6 [48]	S690 (690 MPa)	$\varepsilon_f \geqslant 14\%$
Japan	JIS G 3128 [60]	SHY685 (685 MPa)	$\varepsilon_f \geqslant 16\%$
	JIS G 3140 [61]	SBHS700 (700 MPa)	$\varepsilon_f \geqslant 16\%$
	JIS G 3114 [62]	SMA570W/570P (460 MPa)	$\varepsilon_f \geqslant 19\%$
	JIS G 3101 [31]	SS540 ($\geqslant$ 400 MPa)	$\varepsilon_f \geqslant 16\%$
U.S.	ASTM A1011/A1011M [63]	UHSS 100 (690 MPa)	$\varepsilon_{f,50} \geqslant 12\%$
	A514/514M [64]	HPS 100W (690 MPa)	$\varepsilon_{f,50} \geqslant 14\%$
	A572/572M [65]	HSLA (690 MPa)	$\varepsilon_{f,50} \geqslant 18\%$

Table 6 Averaged test results of the flat coupon taken from the HSS parent plates.

Section	$E_{s,p}$ (GPa)	v	$f_{y,p}$ (Mpa)	$f_{u,p}$ (Mpa)	$\varepsilon_{u,p}$ (%)	$\varepsilon_{f,p}$ (%)	$\varepsilon_{sh,p}$ (%)
6 mm plate	214.1	0.29	768.5	816.2	6.45	14.95	1.98
10 mm plate	216.1	0.30	791.3	825.6	6.55	16.18	2.32

Table 7 Test results of the material properties within the cold-formed section CF1-145×6-1.75.

Section	E_s (GPa)	f_y (MPa)	f_u (MPa)	ε_u (%)	$\varepsilon_{f,25ex}$ (%)	ε_f (%)	ε_{sh} (%)	$f_{0.05}$ (MPa)
CF1-145×6-1.75-W1	172.5	645	808	9.1	19.2	18.5	-[a]	-[b]
CF1-145×6-1.75-F2	205.1	787	825	6.7	15.8	16.2	2.12	-[b]
CF1-145×6-1.75-F3	214.2	785	824	6.9	16.3	16.5	2.07	-[b]
CF1-145×6-1.75-F4	206.2	792	832	6.4	15.8	16.3	-[a]	785
CF1-145×6-1.75-C5	197.5	827	873	1.9	11.5	12.6	-[a]	775
CF1-145×6-1.75-F6	210.5	782	826	6.8	16.2	15.8	-[a]	771
CF1-145×6-1.75-C7	191.2	846	895	1.5	10.2	11.8	-[a]	796
CF1-145×6-1.75-F8	212.6	789	831	6.5	15.6	15.4	-[a]	776

Note: [a] indicates the strain hardening was not observed from the tensile coupon test. [b] indicates that the 0.05% proof strength is not applicable to the coupon with either welding materials or yield plateau

Table 8 Test results of the material properties within the cold-formed section CF2-145×6-1.75.

Section	E_s (GPa)	f_y (MPa)	f_u (MPa)	ε_u (%)	$\varepsilon_{f,25ex}$ (%)	ε_f (%)	ε_{sh} (%)	$f_{0.05}$ (MPa)
CF2-145×6-1.75-W1	172.6	658	842	6.7	10.8	12.3	-[a]	-[b]
CF2-145×6-1.75-F2	198.2	796	831	6.5	16.3	15.8	1.85	-[b]
CF2-145×6-1.75-C3	195.6	840	885	1.8	12.3	14.2	-[a]	778
CF2-145×6-1.75-F4	219.1	793	843	6.5	15.8	16.3	-[a]	791
CF2-145×6-1.75-F5	204.6	772	821	6.6	16.3	15.6	-[a]	765
CF2-145×6-1.75-C6	192.2	843	898	1.6	10.8	11.8	-[a]	772

Note: [a] indicates the strain hardening was not observed from the tensile coupon test. [b] indicates that the 0.05% proof strength is not applicable to the coupon with either welding materials or yield plateau

Table 9 Test results of the material properties within the cold-formed section CF2-220×6-2.00.

Section	E_s (GPa)	f_y (MPa)	f_u (MPa)	ε_u (%)	$\varepsilon_{f,25ex}$ (%)	ε_f (%)	ε_{sh} (%)	$f_{0.05}$ (MPa)
CF2-220×6-2.00-W1	190.3	662	838	8.5	18.6	17.8	-[b]	-[c]
CF2-220×6-2.00-F2	212.2	750	800	6.1	15.8	16.2	2.15	-[c]
CF2-220×6-2.00-F3	207.5	768	816	6.0	-[a]	15.2	-[b]	766
CF2-220×6-2.00-C4	195.6	799	849	1.6	13.5	13.2	-[b]	741
CF2-220×6-2.00-F5	211.4	765	819	6.4	17.5	16.3	-[b]	761
CF2-220×6-2.00-F6	211.7	780	831	6.4	17.2	17.6	-[b]	774
CF2-220×6-2.00-C7	196.2	818	868	1.7	12.2	13.5	-[b]	759

Note: [a] indicates the occurrence of the fracture is located outside the range of the extensometer gauge length. [b] indicates the strain hardening was not observed from the tensile coupon test. [c] indicates that the 0.05% proof strength is not applicable to the coupon with either welding materials or yield plateau.

Table 10 Test results of the material properties within the cold-formed section CF2-145×10-1.75.

Section	E_s (GPa)	f_y (MPa)	f_u (MPa)	ε_u (%)	$\varepsilon_{f,50ex}$ (%)	ε_f (%)	ε_{sh} (%)	$f_{0.05}$ (MPa)
CF2-145×10-1.75-W1	175.8	645	842	7.8	22.7	19.2	-[a]	-[b]
CF2-145×10-1.75-F2	211.1	776	817	5.8	16.3	16.8	-[a]	775
CF2-145×10-1.75-F3	211.0	797	836	6.4	17.7	16.5	2.41	-[b]
CF2-145×10-1.75-C4	198.8	802	845	1.9	11.9	12.5	-[a]	743
CF2-145×10-1.75-F5	210.1	795	833	6.5	18.4	17.1	2.40	-[b]
CF2-145×10-1.75-F6	216.0	799	839	6.3	-[#]	16.6	2.35	-[b]
CF2-145×10-1.75-C7	199.5	810	863	1.8	13.1	14.8	-[a]	757

Note: [a] indicates the occurrence of the fracture is located outside the range of the extensometer gauge length. [b] indicates the strain hardening was not observed from the tensile coupon test. [c] indicates that the 0.05% proof strength is not applicable to the coupon with either welding materials or yield plateau.

Table 11 Measured material properties from corner coupon specimens and the predicted values using different methods.

Specimen	Experimental results			Prediction by Karren [68]		Prediction by Pham et al. [69]		Prediction by Gardner et al. [70]	
	f_y (MPa)	f_u (MPa)	$\frac{f_u}{f_y}$	$f_{y,c,karren\&AISI}$ (MPa) Eq. (1), (2), (3)	$\frac{f_{y,ckarren\&AISI}}{f_y}$	$f_{y,c,Pham}$ (MPa) Eq. (1), (4), (5)	$\frac{f_{y,,c,Pham}}{f_y}$	$f_{y,c,Gardner}$ (MPa) Eq. (1), (6), (7)	$\frac{f_{y,c,Gardner}}{f_y}$
CF1-145×6-1.75-C5	827	872	1.05	849.2	1.027	906.0	1.096	750.1	0.907
CF1-145×6-1.75-C7	846	895	1.06	873.0	1.032	928.5	1.097	769.7	0.910
CF2-145×6-1.75-C3	840	885	1.05	861.4	1.026	919.9	1.095	761.3	0.906
CF2-145×6-1.75-C6	843	898	1.07	879.0	1.043	928.5	1.101	772.0	0.916
CF2-220×6-2.00-C4	798	849	1.06	830.5	1.041	878.4	1.101	729.9	0.915
CF2-220×6-2.00-C7	818	868	1.06	848.0	1.037	899.2	1.099	746.4	0.912
CF2-145×10-1.75-C4	802	845	1.05	822.5	1.026	878.3	1.095	726.9	0.906
CF2-145×10-1.75-C7	810	863	1.07	844.8	1.043	892.2	1.102	741.9	0.916
				Mean	1.034	Mean	1.098	Mean	0.911
				CoV	0.006	CoV	0.002	CoV	0.003

Table 12 The dimensions of the tensile coupons prepared for DIC measurement.

Section	t (mm)	L_t (mm)	L_c (mm)	L_o (mm)	w (mm)	r (mm)	G_w (mm)	G_l (mm)
CF2-145×6-1.75-F2-D	5.85	177.2	35	25	4.1	12.5	20.1	60.2
CF2-145×6-1.75-F4-D	5.82	176.8	35	25	3.9	12.5	20.2	60.3
CF2-145×10-1.75-F3-D	9.62	212.1	70	50	8.2	12.5	30.2	60.1
CF2-145×10-1.75-F6-D	9.64	212.3	70	50	7.9	12.5	29.9	60.4

Table 13 The results of DIC measurements.

Section	Full life-cycle deformation stages									
	Yielding		Onset of diffuse necking		Diffuse necking I		Diffuse necking II		Localized necking	
	ε_t (%)	ε (%)	ε_t (%)	ε (%)	ε_t (%)	ε (%)	ε_t (%)	ε (%)	ε_t (%)	ε (%)
CF2-145×6-1.75-F2D	0.64	0.64	7.6	7.6	26	8.2	48	9.4	90	16.6
CF2-145×6-1.75-F4D	0.60	0.60	7.1	7.2	25	7.9	50	9.5	89	16.9
CF2-145×10-1.75-F3D	0.64	0.63	6.8	6.9	27	7.6	49	9.3	91	16.2
CF2-145×10-1.75-F6D	0.57	0.57	7.1	7.4	26	7.8	47	9.2	92	15.8